DISEASES AND DISORDERS

Maintaining hypoxia environment of subchondral bone alleviates osteoarthritis progression

Hao Zhang[1,2,3]†, Lipeng Wang[2]†, Jin Cui[1,2]†, Sicheng Wang[2,4]†, Yafei Han[2], Hongda Shao[5], Cheng Wang[5], Yan Hu[2,3], Xiaoqun Li[1,6], Qirong Zhou[1], Jiawei Guo[1,2], Xinchen Zhuang[1], Shihao Sheng[1], Tao Zhang[1], Dongyang Zhou[2], Jiao Chen[2], Fuxiao Wang[2], Qianmin Gao[2], Yingying Jing[2]*, Xiao Chen[1,3]*, Jiacan Su[1,2,3]*

Abnormal subchondral bone remodeling featured by overactivated osteoclastogenesis leads to articular cartilage degeneration and osteoarthritis (OA) progression, but the mechanism is unclear. We used lymphocyte cytosolic protein 1 (*Lcp1*) knockout mice to suppress subchondral osteoclasts in a mice OA model with anterior cruciate ligament transection (ACLT), and *Lcp1*$^{-/-}$ mice showed decreased bone remodeling in subchondral bone and retarded cartilage degeneration. For mechanisms, the activated osteoclasts in subchondral bone induced type-H vessels and elevated oxygen concentration, which ubiquitylated hypoxia-inducible factor 1 alpha subunit (HIF-1α) in chondrocytes and led to cartilage degeneration. *Lcp1* knockout impeded angiogenesis, which maintained hypoxia environment in joints and delayed the OA progression. Stabilization of HIF-1α delayed cartilage degeneration, and knockdown of *Hif1a* abolished the protective effects of *Lcp1* knockout. Last, we showed that Oroxylin A, an *Lcp1*-encoded protein L-plastin (LPL) inhibitor, could alleviate OA progression. In conclusion, maintaining hypoxic environment is an attractive strategy for OA treatment.

INTRODUCTION

Osteoarthritis (OA) is a complex disease affecting the whole joint, characterized by cartilage degeneration, aberrant bone remodeling, osteophyte formation, and joint inflammation (*1*). As the leading cause of disability and pain, OA affects more than 300 million people worldwide (*2*). The current treatment algorithm including self-education and cycloxygenase-2 inhibitors mainly helps symptom alleviation, and no disease-modifying OA drug is available due to the limited understanding of OA pathogenesis (*3*).

OA is featured by subchondral bone changes in clinical findings (*4*). Subchondral bone subjacent to cartilage provides nutritional and mechanical support for cartilage (*5*). Subchondral bone marrow edema, formation of osteocysts, and sclerosis could be found in most patients with OA. Subchondral bone marrow edema first appears in magnetic resonance imaging (MRI) images followed by osteocyst formation in early patients with OA, and the subchondral bone marrow edema area in MRI corresponds to the degenerated cartilage above (*6*). The roles of subchondral bone in OA progression remain unclear.

Overactivated osteoclasts in subchondral bone are closely associated with OA progression (*7*). Physiologically, the bone remodeling activity and number of osteoclasts are strictly controlled in the subchondral bone, and the number of osteoclasts markedly increases at the early stage of OA mice model (*8*, *9*). Several hypotheses regarding osteoclast roles in OA have been proposed. Osteoclast precursors migrate into the cartilage layer and directly contact with hypertrophic chondrocytes to degrade the osteochondral junction and articular cartilage (*10*, *11*). Growth factors released from the bone matrix through osteoclastic bone resorption including transforming growth factor beta 1, insulin-like growth factor 1, and platelet-derived growth factor BB (PDGF-BB) regulate chondrocyte metabolism (*12*, *13*). Nevertheless, the number of osteoclasts notably drops after reaching the peak in OA models, but the cartilage degeneration continuously deteriorates. Thus, the roles of osteoclasts in cross-talk between subchondral bone and chondrocytes remain mysterious.

Lacking blood vessels, subchondral bone, and cartilage remain hypoxic, which is vital for chondrocyte homeostasis (*14*). Hypervascularization in subchondral bone is the hallmark and drug target of OA progression. Angiogenesis stimulated by elevated PDGF-BB in subchondral bone contributes to OA development (*13*). Administration of bevacizumab, a vascular endothelial growth factor blocker, inhibits angiogenesis and mitigates OA (*15*). Thus, we hypothesize that blood vessel formation induced by osteoclasts in subchondral bone in early stage of OA alters the joint hypoxia environment and contributes to sustained cartilage degeneration.

In this study, we used *Lcp1* knockout mice with impaired osteoclast formation as we previously reported and established OA model with anterior cruciate ligament transection (ACLT) (*16*). *Lcp1*$^{-/-}$ mice after ACLT showed preserved articular cartilage and delayed OA progression. Mechanistically, angiogenesis by osteoclast activation elevated the concentration of O_2 in subchondral bone and cartilage. The disrupted joint hypoxia environment with elevated oxygen partial pressure promoted chondrocyte degeneration by abolishing hypoxia-inducible factor 1 alpha subunit (HIF-1α) functions, and stabilizing HIF-1α functions prevented cartilage destruction.

[1]Department of Orthopedics, Shanghai Changhai Hospital, Naval Medical University, Shanghai 200433, China. [2]Institute of Translational Medicine, Shanghai University, Shanghai 200444, China. [3]Department of Orthopedic, Xin Hua Hospital, Shanghai Jiao Tong University School of Medicine, Shanghai 200092, China. [4]Department of Orthopedics, Shanghai Zhongye Hospital, Shanghai 200941, China. [5]Department of Nuclear Medicine, Ren Ji Hospital, Shanghai Jiao Tong University School of Medicine, Shanghai 200127, China. [6]Department of Orthopedics, No. 929 Hospital, Naval Medical University, Shanghai 200433, China.
†These authors contributed equally to this work.
*Corresponding author. Email: jingy4172@shu.edu.cn (YY.J.); sirchenxiao@126.com (X.C.); drsujiacan@163.com (JC.S.)

RESULTS

Plastin up-regulated in subchondral bone correlates with increased osteoclast activity in early OA

To investigate the involvement of osteoclasts and L-plastin (LPL) in OA, we analyzed the micro–computed tomography (micro-CT) and knee section of wild-type (WT) mice after ACLT at different time points. The cartilage degeneration kept progressing during 8 weeks with the arising OA Research Society International (OARSI) grade (Fig. 1, A and B). During OA progression, the thickness of hyaline cartilage (HC) decreased, while the thickness of calcified cartilage (CC) gradually duplicated, and the ratio of HC/CC decreased to an average of 0.81 at 8 weeks (fig. S1, A and B). The bone mass of subchondral bone decreased at 2 weeks after ACLT with bone volume/total volume (BV/TV) ranging from 34.3 to 55.8%, but BV/TV increased to 56.6 to 76.2% at 4 and 8 weeks after ACLT (Fig. 1, C and D). The images of whole-joint micro-CT three-dimensional (3D) reconstruction showed large osteophytes formed in 8 weeks after ACLT (fig. S1, C and D). The changes of subchondral bone plate thickness (SBP.th), trabecular spacing (Tb.sp), and trabecular bone pattern factor (Tb.pf) were consistent with this trend (Fig. 1F and fig. S1, F and H). Correspondingly, the number of tartrate-resistant acid phosphatase–positive ($TRAP^+$) cells increased rapidly during the first 2 weeks after ACLT to the peak of an average of 13.4 cells/mm^2 and decreased after 2 weeks (Fig. 1, E and G). LPL is exclusively expressed in myeloid lineage cells and is vital for osteoclast fusion and mature osteoclast formation (*16*). No LPL^+ cell was observed in cartilage. Few were found surrounding subchondral trabecular bone, and abundant cells were detected around the primary spongiosa near epiphysis in sham mouse (fig. S1E). Two weeks after ACLT, an increased number of LPL^+ cells were observed around the subchondral trabecular bone but not in cartilage (fig. S1G). The immunohistochemistry results showed that the number of LPL^+ cells in subchondral bone was consistent with that of $TRAP^+$ cells, reaching the peak of an average of 10.8 cells/mm^2 (Fig. 1, H and I). The immunofluorescence results of LPL and TRAP showed that the number of LPL^+ and $TRAP^+$ cells in subchondral bone reached the peak of an average of 14.6 cells/mm^2 at 2 weeks after ACLT and decreased to baseline at 8 weeks (Fig. 1, J and K). Together, under physiological condition, nearly no LPL^+ or $TRAP^+$ cells could be detected in subchondral bone. While 2 weeks after ACLT, the number of LPL^+ and $TRAP^+$ cells is significantly increased, indicating an accelerated bone remodeling in subchondral bone in early stage of OA.

Lcp1 knockout reduces subchondral bone resorption and ameliorates articular cartilage degeneration

To explore the role of LPL in OA progression, we generated $Lcp1^{-/-}$ mice by deleting exon4 of *Lcp1* (fig. S2, A and B). The success of *Lcp1* knockout was verified both at the gene and transcriptional level (fig. S2, C to E). Although mutated segment of *Lcp1* could express, the mutated protein does not have normal functions according to our previous research (*16*). Micro-CT results showed that the BV/TV in subchondral bone of *Lcp1* knockout mice increased to an average of 75.1 and 81.9% compared to their littermates of an average of 55.8 and 67.4% at 2 and 4 weeks after ACLT (Fig. 2, A and B). The Tb.sp. and Tb.pf in subchondral bone of *Lcp1* knockout mice decreased compared to the WT mice at 2 weeks after ACLT (fig. S3, A and B). There was no statistical difference in SBP.th between the two groups (Fig. 2C). As our previous study showed, the number of $TRAP^+$ cells in subchondral bone in *Lcp1* knockout mice was almost half of that (53.7 and 54.2%) in WT group at 2 and 4 weeks after ACLT (Fig. 2, D and E). The results of Safranin O/fast green staining showed that the OARSI grade increased at 4 and 8 weeks after ACLT in WT mice. *Lcp1* knockout decreased 1.25- and 2.25-fold compared with WT mice (Fig. 2, F and G). The ratio of HC/CC showed a 1.42- and 1.71-fold increase in *Lcp1* knockout mice at 4 and 8 weeks after ACLT compared to that of WT mice (fig. S3, C and D). The area of Collagen Type II positive ($COL\ II^+$) region (Fig. 2, H and I) and Aggrecan positive ($ACAN^+$) region (fig. S3, E and F) in *Lcp1* knockout mice were 10.5 to 85.6% higher than that in WT mice. The area of matrix metalloproteinase 13–positive ($MMP13^+$) region (Fig. 2, J and K), A Disintegrin And Metalloproteinase With Thrombospondin Motifs 5 positive ($ADAMTS5^+$) region (fig. S3, G and H), and $COL\ X^+$ region (fig. S3, I and J) in *Lcp1* knockout mice were 3 to 24.5% decreased compared to that of WT mice after ACLT. As osteoclasts mediated sensory nerve innervation in subchondral bone and pain in OA, we evaluated the effects of *Lcp1* deletion in sensory innervation and pain (*17*). The results showed that the level of NETRIN-1 increased at 2 weeks after ACLT in WT mice. However, the expression of NETRIN-1 in subchondral bone was not observed in *Lcp1* knockout mice (fig. S4, A and B). Correspondingly, the number of Calcitonin gene-related peptide ($CGRP^+$) nerve fibers in $Lcp1^{-/-}$ mice were 0.72- and 0.57-fold lower when compared to their littermates (fig. S4, C and D). The von Frey test showed that the threshold of paw withdrawal showed a 1.7- to 2.6-fold increase in *Lcp1* knockout mice compared to control mice 3 weeks after ACLT (fig. S4E). To sum up, *Lcp1* knockout alleviates OA progression featured by retarded subchondral bone resorption, alleviated articular cartilage degeneration, and improved pain.

Lcp1 knockout impairs angiogenesis and maintains a low pO_2 of subchondral bone and cartilage

Under physiological condition, because of the lack of blood vessels, the O_2 concentration in cartilage is strictly maintained at a very low level, as hypoxia is vital for chondrocyte survival and homeostasis (*18*). Osteoclasts mediate the type-H vessel formation, which provides rich oxygen in subchondral bone after ACLT (*19*). We hypothesized that *Lcp1* knockout inhibited osteoclast-induced angiogenesis and blocked the diffusion of oxygen from subchondral bone to cartilage. To test this hypothesis, we first performed the microangiography of subchondral bone, and the results showed that the volume of vessel increased 1.56- and 1.62-fold in WT mice at 4 and 8 weeks after ACLT. In contrast, the vessel volume did not notably change in $Lcp1^{-/-}$ mice after ACLT (0.95- and 1.14-fold compared to sham group) (Fig. 3, A and B). Next, we evaluated the level of $CD31^{hi}EMCN^{hi}$ vessels. Consistent with the level of vessel volume, the number of CD31 and endomucin (EMCN)–positive cells notably increased to an average of 20.4 and 23.1 cells/mm^2 in WT mice at 4 and 8 weeks after ACLT but increased to an average of 12.9 and 15.2 cells/mm^2 in *Lcp1* deletion after ACLT (Fig. 3, C and D). Next, we measured hypoxic status in subchondral bone and cartilage using hypoxia probe. The results of pimonidazole immunostaining, an indicator of hypoxia, revealed that the fluorescence intensity of pimonidazole decreased 33.2 and 81.0% in WT mice at 4 and 8 weeks after ACLT. The fluorescence intensity was

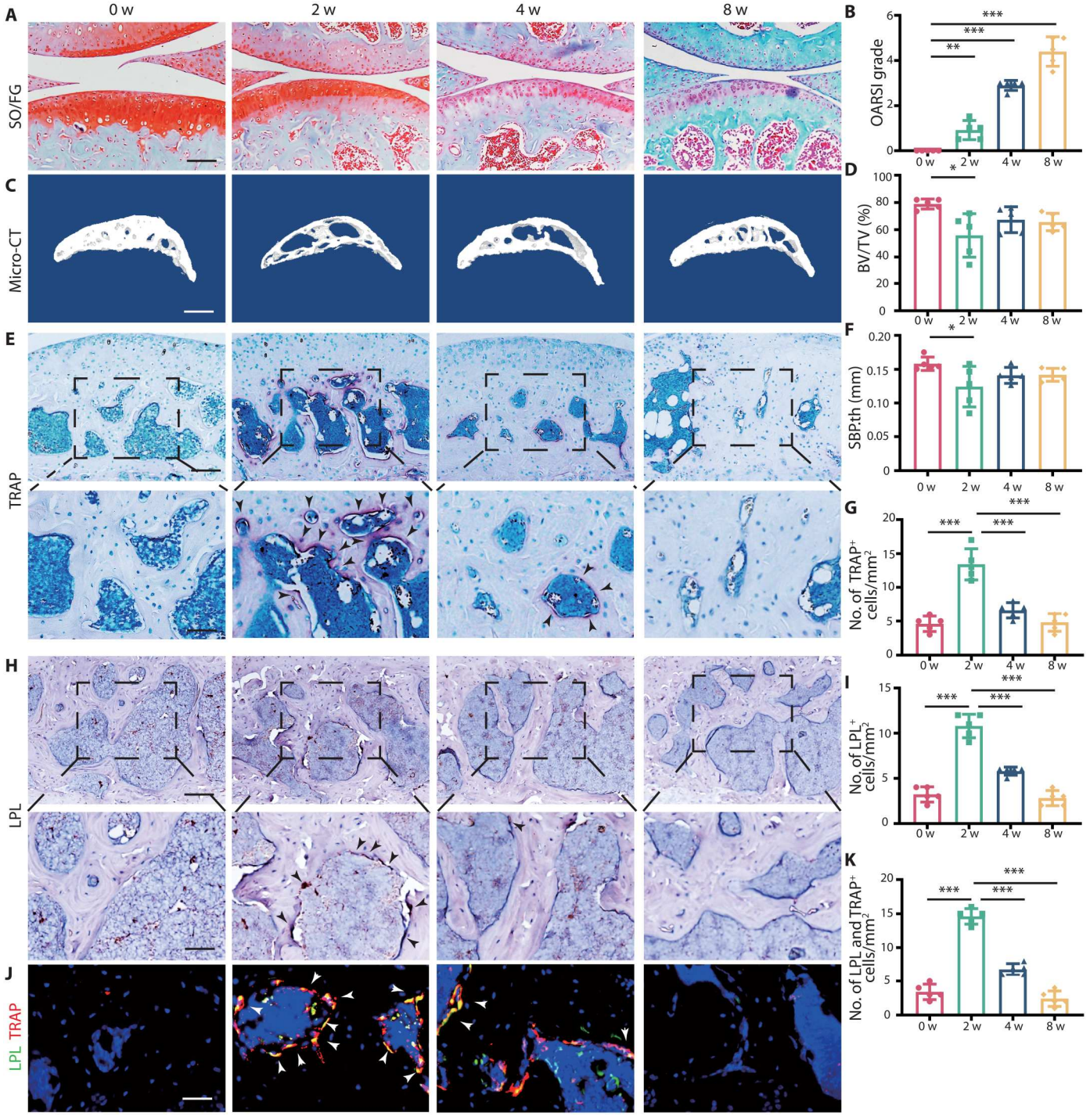

Fig. 1. L-Plastin up-regulated in subchondral bone correlates with increased osteoclast activity in early stage of OA. (**A**) Safranin O/fast green (SO/FG) staining of knee articular cartilage at 0, 2, 4, and 8 weeks after operation. Scale bar, 100 μm. (**B**) OARSI grade of knee articular cartilage. (**C**) Three-dimensional images of the sagittal plane of medial tibial subchondral bone at 0, 2, 4, and 8 weeks after ACLT. Scale bar, 500 μm. (**D**) Micro-CT quantitative analysis of tibial subchondral bone, BV/TV (%). (**E**) TRAP staining image of tibial subchondral bone at 0, 2, 4, and 8 weeks after ACLT. Scale bar, 100 (top) and 50 μm (bottom). (**F**) Micro-CT quantitative analysis of tibial subchondral bone, SBP.th (mm). (**G**) Quantitative analysis of TRAP-positive cells in subchondral bone marrow. (**H**) Representative images of LPL protein immunohistochemistry in tibial subchondral bone at 0, 2, 4, and 8 weeks after ACLT. Scale bar, 100 (top) and 50 μm (bottom). (**I**) Quantitative analysis of LPL^+ osteoclast in subchondral bone marrow. (**J**) Representative images of the double staining of LPL and TRAP in tibial subchondral bone at 0, 2, 4, and 8 weeks after ACLT. Scale bar, 50 μm. (**K**) Quantitative analysis of LPL^+ osteoclasts in subchondral bone. $n = 5$ per group. $^*P < 0.05$, $^{**}P < 0.01$, and $^{***}P < 0.001$.

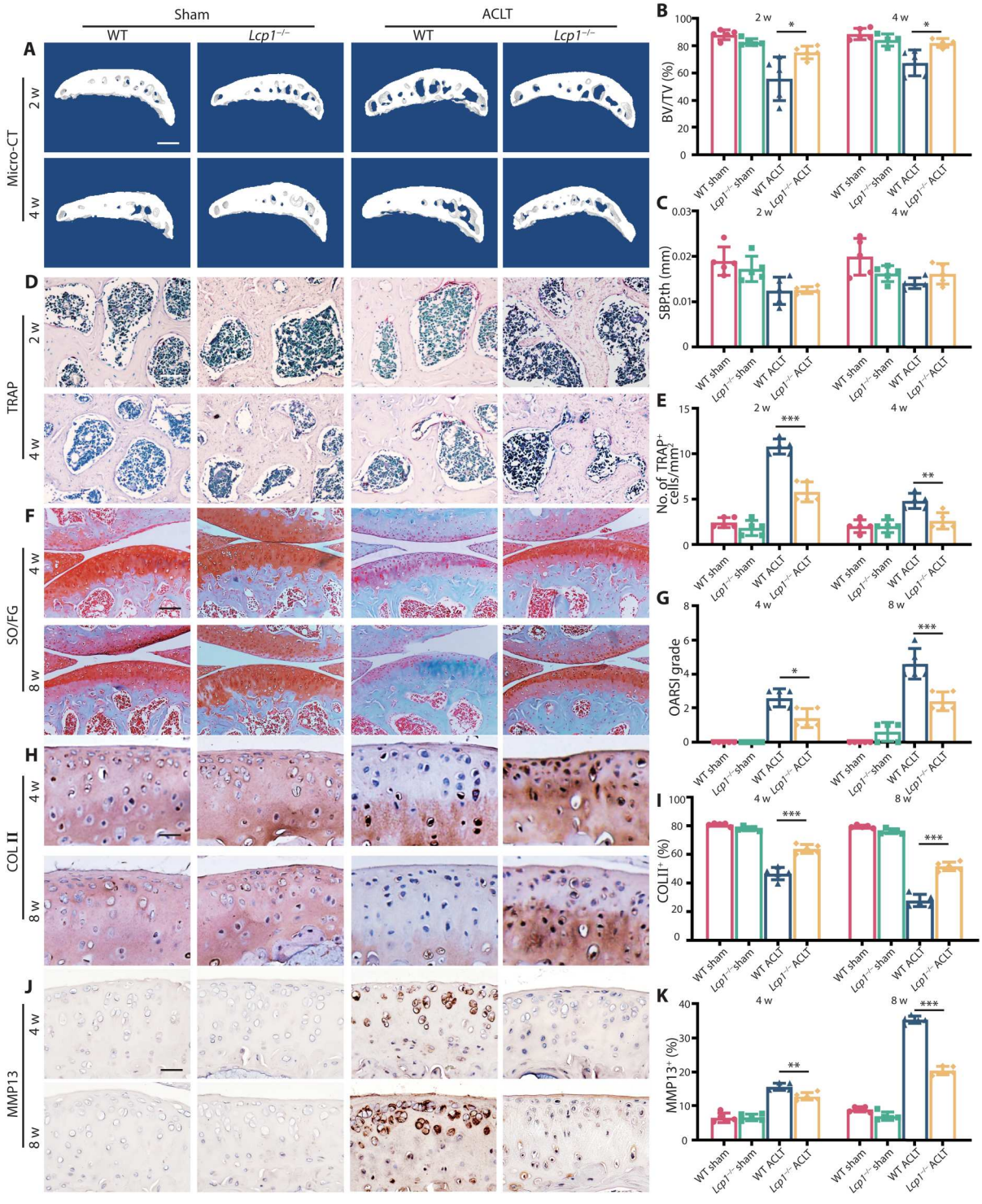

Fig. 2. Subchondral bone resorption and articular cartilage degeneration are retarded in *Lcp1* knockout mice. (**A**) Representative micro-CT 3D images of tibia subchondral bone of *Lcp1*$^{-/-}$ mice and WT littermates at 2 and 4 weeks after ACLT. Scale bar, 500 μm. (**B** and **C**) Micro-CT quantitative analysis of tibial subchondral bone: BV/TV (%) (B) and SBP.th (mm) (C). (**D**) TRAP staining image of tibial subchondral bone of *Lcp1*$^{-/-}$ mice and WT littermates at 2 and 4 weeks after ACLT. Scale bar, 50 μm. (**E**) Quantitative analysis of TRAP^{+} cells in subchondral bone marrow between *Lcp1*$^{-/-}$ mice and WT littermates. (**F**) Safranin O/Fast Green staining of *Lcp1*$^{-/-}$ mice and WT littermates' knee articular cartilage. Scale bar, 100 μm. (**G**) OARSI grade of knee articular cartilage. (**H**) Representative images of COL II immunohistochemistry in tibial articular cartilage of LPL$^{-/-}$ mice and WT littermates at 4 and 8 weeks after ACLT. Scale bar, 20 μm. (**I**) Quantitative analysis of COL II^{+} area in articular cartilage. (**J**) Representative images of MMP13 immunohistochemistry in tibial articular cartilage of *Lcp1*$^{-/-}$ mice and WT littermates at 4 and 8 weeks after ACLT. Scale bar, 20 μm. (**K**) Quantitative analysis of MMP13^{+} area in articular cartilage. $n = 5$ per group. *$P < 0.05$, **$P < 0.01$, and ***$P < 0.001$.

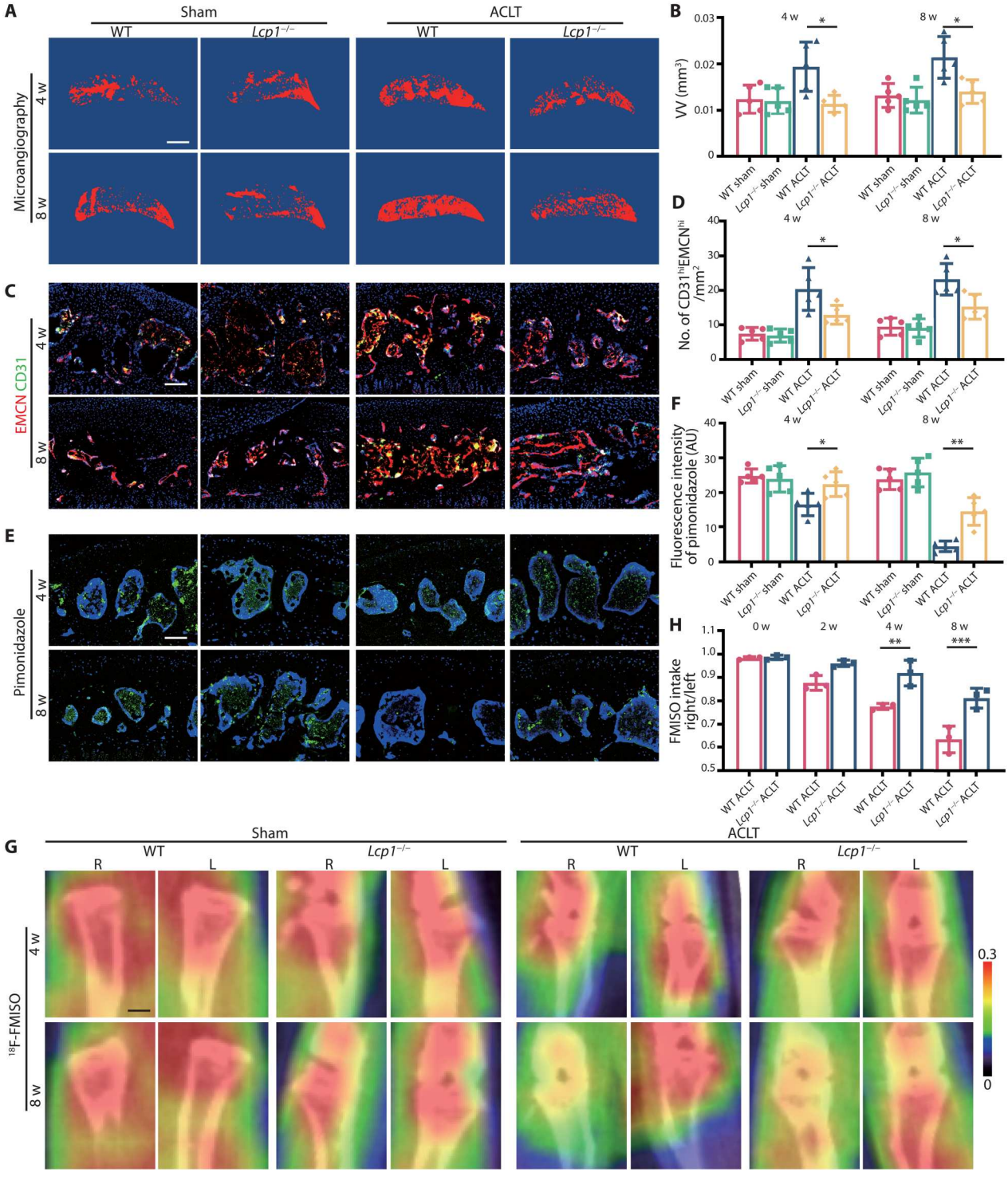

Fig. 3. *Lcp1* knockout impairs angiogenesis and maintains a low pO2 of subchondral bone and cartilage. (**A**) 3D image of the sagittal plane of CT-based microangiography in medial tibial subchondral bone of *Lcp1*$^{-/-}$ mice and WT mice at 4 and 8 weeks after ACLT. Scale bar, 500 μm. (**B**) Quantification of vessel volume (VV) in medial tibial subchondral bone. (**C**) Maximum intensity projections of immunostaining of endomucin (EMCN) (red), CD31 (green), and Emcn^{hi}CD31^{hi} (yellow) cells in medial tibial subchondral bone of *Lcp1*$^{-/-}$ mice and WT mice at 4 and 8 weeks after operation. Scale bar, 100 μm. (**D**) Quantification of CD31 and EMCN-positive cells in subchondral bone marrow. (**E**) Immunostaining of pimonidazole (green) in medial tibial subchondral bone of *Lcp1*$^{-/-}$ mice and WT mice at 4 and 8 weeks after ACLT. Scale bar, 100 μm. (**F**) Quantification of pimonidazole fluorescence intensity in subchondral bone marrow. R, right; L, left. AU, arbitrary units. (**G**) ^{18}F-FMISO–based PET/CT images of *Lcp1*$^{-/-}$ mice and WT mice at 4 and 8 weeks after ACLT. Scale bar, 1 mm. (**H**) Quantification of right knee maximum ^{18}F-FMISO uptake/left knee maximum ^{18}F-FMISO uptake. $n = 5$ per group. *$P < 0.05$, **$P < 0.01$, and ***$P < 0.001$.

maintained in *Lcp1*$^{-/-}$ mice, and the intensity of sham group remained 93.6 and 56.4% at 4 and 8 weeks (Fig. 3, E and F). Although synovial inflammation is not the main manifestation in OA, the knockout of *Lcp1* also decreased the synovial inflammation in progressed OA (fig. S5, A and B). To explore the effect of synovial membrane on the hypoxia conditions of the cartilage, we analyzed the type-H vessels and pimonidazole staining of the synovium. Four weeks after ACLT operation, the level of pimonidazole in joint was significantly decreased, and the number of the type-H vessels was increased in subchondral bone (fig. S5, C to H). However, the intensity of pimonidazole and H-type vessels showed no significant change in synovium at this time point, indicating that synovium could not play a leading role in altering the hypoxia state of the cartilage. The knockout of *Lcp1* showed no significant effect on the type-H vessels or pimonidazole fluorescence in synovium at 4 weeks after ACLT. However, the level in the whole joint had been substantially changed (fig. S5, C to H). The above results implied that the increase of partial pressure of oxygen (pO_2) in the whole joint during OA was mainly attributed to the subchondral bone rather than synovium. To further confirm these results, we directly measured the O_2 levels in the joint in living mice with ^{18}F-fluoromisonidazole (^{18}F-FMISO)–based positron emission tomography (PET)/CT. Higher ^{18}F-FMISO intake indicated lower pO_2 in tissue. The ratio of right (ACLT) and left knee (sham) uptake of ^{18}F-FMISO in WT mice was lower than in *Lcp1*$^{-/-}$ mice from 2 weeks after ACLT. At 8 weeks, uptake of ^{18}F-FMISO in WT right knee were only 57 to 68% of left knee, but ^{18}F-FMISO uptake in *Lcp1*$^{-/-}$ mice right knee was 76 to 84% of normal side, indicating that the up-regulation of pO_2 in OA progression was retarded after *Lcp1* knockout (Fig. 3, G and H). Together, *Lcp1* knockout impedes the formation of type-H vessels and maintains the hypoxic environment in subchondral bone and cartilage.

HIF-1α loss is observed in OA cartilage from human and mice

To explore the mechanism of how pO_2 affects cartilage degeneration, we hypothesized that the O_2 affected cartilage chondrocytes through HIF-1α, a vital transcriptional factor regulated by oxygen for chondrocytes homeostasis. First, we found that the level of HIF-1α decreased after ACLT in WT mice, and the knockout of *Lcp1* could alleviate this decline. Positive area of HIF-1α in *Lcp1* knockout mice were 1.26- and 1.36-fold higher than WT mice at 4 and 8 weeks after ACLT (Fig. 4, A and B). To further confirm the expression of HIF-1α, we collected human articular cartilage in different OARSI grade from patients (Fig. 4C). HIF-1α was abundant in superficial and deep zone in S0 cartilage (80.6 and 75.5%); however, the level substantially decreased when OA progressed (Fig. 4, D and E). In S2 to S4 phases, HIF-1α expression was hardly detected in cartilage. To sum up, the cartilage degeneration is accompanied by the destruction of hypoxia environment and degraded HIF-1α in chondrocyte.

Next, we used single-cell RNA sequencing (RNA-seq) analysis to explore the transcriptional changes of *Hif1*a in each subgroup of human chondrocytes. Ji *et al.* (*20*) performed single-cell RNA-seq of human OA cartilage and identified seven chondrocyte populations. We reanalyzed the data and divided those cells into six groups (fig. S6A), including fibrocartilage chondrocytes (FCs), OA-associated hypertrophic chondrocytes (OA-HTCs), regulatory hypertrophic chondrocytes (rHTCs), prehypertrophic chondrocytes (preHTCs), homeostatic chondrocytes (HomCs), and proliferative chondrocytes (ProCs). HTCs are located in the deepest layer of cartilage and may be affected by oxygen derived from subchondral bone. We focused on HTC and further divided HTC into four clusters (fig. S6B). The results showed that cluster 3 of HTC was different from others and expressed several genes that were responsible for matrix degeneration and endochondral ossification, including *MMP13*, *COL1A1*, *COL10A1*, *VEGFC*, *WNT5A*, and *WNT10B* (fig. S6, C to F). Thus, cluster 3 was termed as OA-HTC. Gene Ontology (GO) analysis results showed that OA-HTC participated in replacement ossification, endochondral bone morphogenesis, bone trabecula morphogenesis, embryonic skeletal system development, and cartilage development involved in endochondral bone morphogenesis (fig. S7A). Kyoto Encyclopedia of Genes and Genomes (KEGG) pathway analysis revealed that extracellular matrix receptor interaction signaling and protein digestion and absorption were activated in OA-HTC (fig. S7B). Other clusters of HTCs were defined as rHTCs as GO analysis results showed that rHTC regulated calcium channel activity and fatty acid transport (fig. S7A). To further identify this HTC subset, we performed immunofluorescence of OA-HTC and rHTC in human and mice cartilage. Wingless-Type MMTV Integration Site Family, Member 5A (WNT5A) and Protein Kinase CGMP-Dependent 2 (PRKG2) were highly expressed in OA-HTC, and Choline Dehydrogenase (CHDH) and Cortactin Binding Protein 2 (CTTNBP2) were collected as markers of rHTC (fig. S6F). CHDH and CTTNBP2 were abundant in deep zone of S0 patients with OA and gradually decreased with the progression of OA, while WNT5A and PRKG2 were mainly expressed in deep zone and CC of S4 patients with OA (fig. S8). Consistent results were also found in ACLT mice (fig. S9), indicating that the OA-HTC is a group of abnormally activated HTCs and only appears in OA sample. The data of Ji *et al.* (*20*) also supported this result that HTC with endochondral ossification function only existed in sample from S4 patients with OA. The gene set variation analysis (GSVA) score of different subsets showed that the HIF-1 signaling pathway was down-regulated by 50% in OA-HTC and FC compared to rHTC, preHTC, and ProC (Fig. 4F). Meanwhile, the OA signaling pathway was activated in OA-HTC, over onefold higher than other four groups (Fig. 4E). These results indicated that the down-regulation of HIF-1 signaling pathway in OA-HTC may be correlated with the up-regulation of OA signaling pathway. To sum up, we speculate that oxygen in subchondral bone degrades HIF-1α in HTC and up-regulates the activation level of OA signaling pathway, which promotes the OA progression.

Knockdown *Hif1a* in articular cartilage partially abolishes the protective effect of *Lcp1* knockout

Next, we explored whether *Lcp1* knockout relieved OA progression through inhibiting HIF-1α degradation. We first confirmed that intraarticular injection of adeno-associated virus (AAV) carrying *Hif1a* knockdown short hairpin RNA (shRNA) was capable of knocking down *Hif1a* in WT and *Lcp1*$^{-/-}$ mice with 86.7 to 89.8% rate (Fig. 5, A and B). The type-H vessel formation in *Lcp1* knockout mice was not affected by *Hif1a* knockdown in cartilage (Fig. 5, C and D). In negative control (NC) group, the OARSI grade of WT mice notably increased 4.6- and 1.91-fold compared to *Lcp1*$^{-/-}$ mice at 4 and 8 weeks after ACLT. After *Hif1a* knocked down, no significant difference was showed between WT

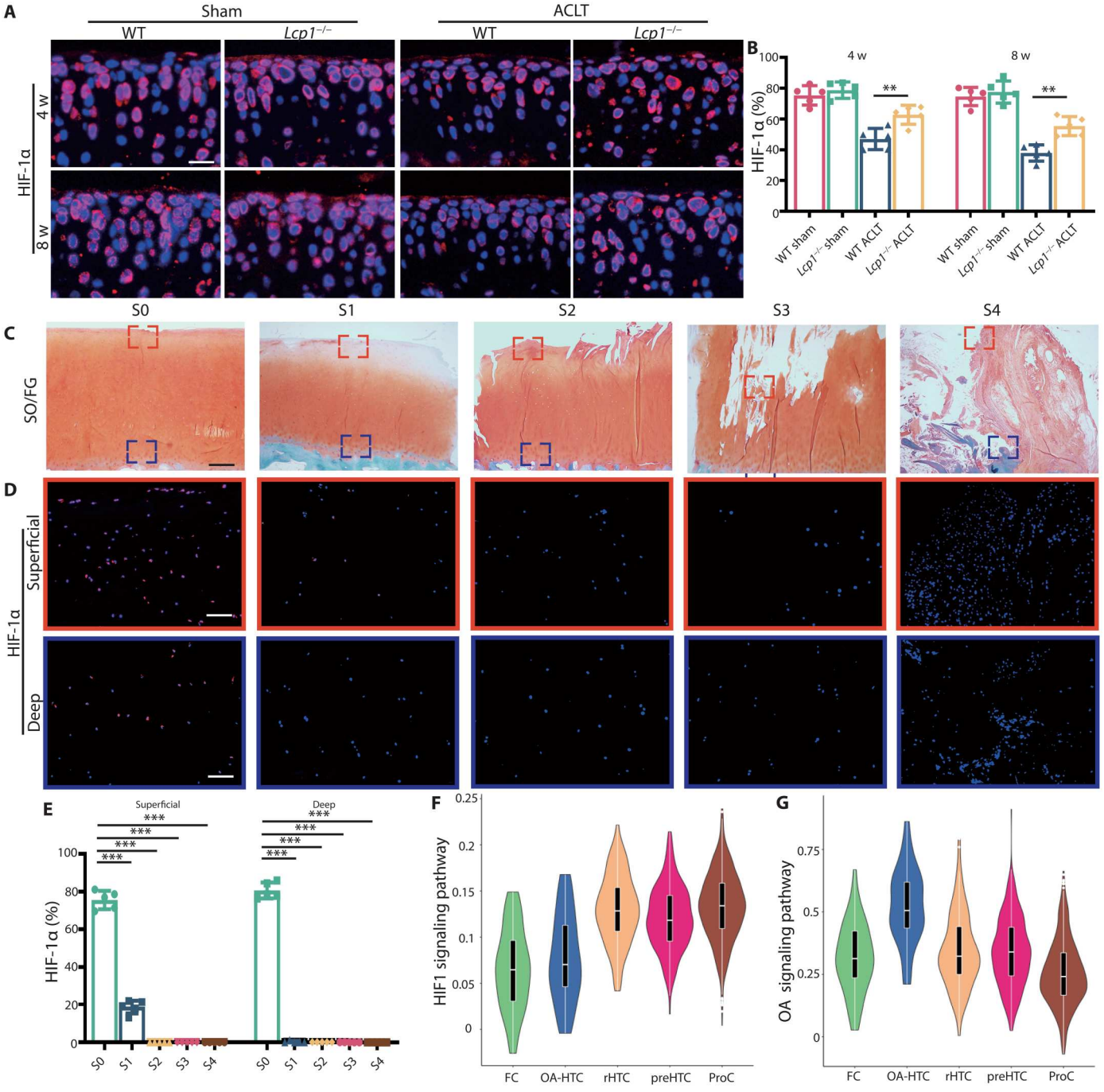

Fig. 4. HIF-1α loss is observed in OA cartilage from human and mice. (**A**) Immunofluorescence staining of HIF-1α in articular cartilage of *Lcp1*$^{-/-}$ mice and WT littermates at 4 and 8 weeks after ACLT. Scale bar, 20 μm. (**B**) Quantitative analysis of HIF-1α fluorescence intensity in *Lcp1*$^{-/-}$ and WT mice articular cartilage. (**C**) Safranin O/fast green staining of human tibia articular cartilage in different OARSI grades. Scale bar, 400 μm. (**D**) Immunofluorescence staining of HIF-1α in human tibia articular cartilage with different OARSI grades. Scale bar, 100 μm. (**E**) Quantitative analysis of HIF-1α fluorescence intensity in human articular cartilage with different OARSI grades. (**F** and **G**) Violin plots showing the GSVA score of HIF1 and OA signaling pathway in five major cell types. $n = 5$ per group. $^{**}P < 0.01$ and $^{***}P < 0.001$. FC, fibrocartilage chondrocyte; preHTC, prehypertrophic chondrocyte; rHTC, regulatory hypertrophic chondrocyte; OA-HTC, OA-associated hypertrophic chondrocyte; ProHTC, proliferative chondrocyte.

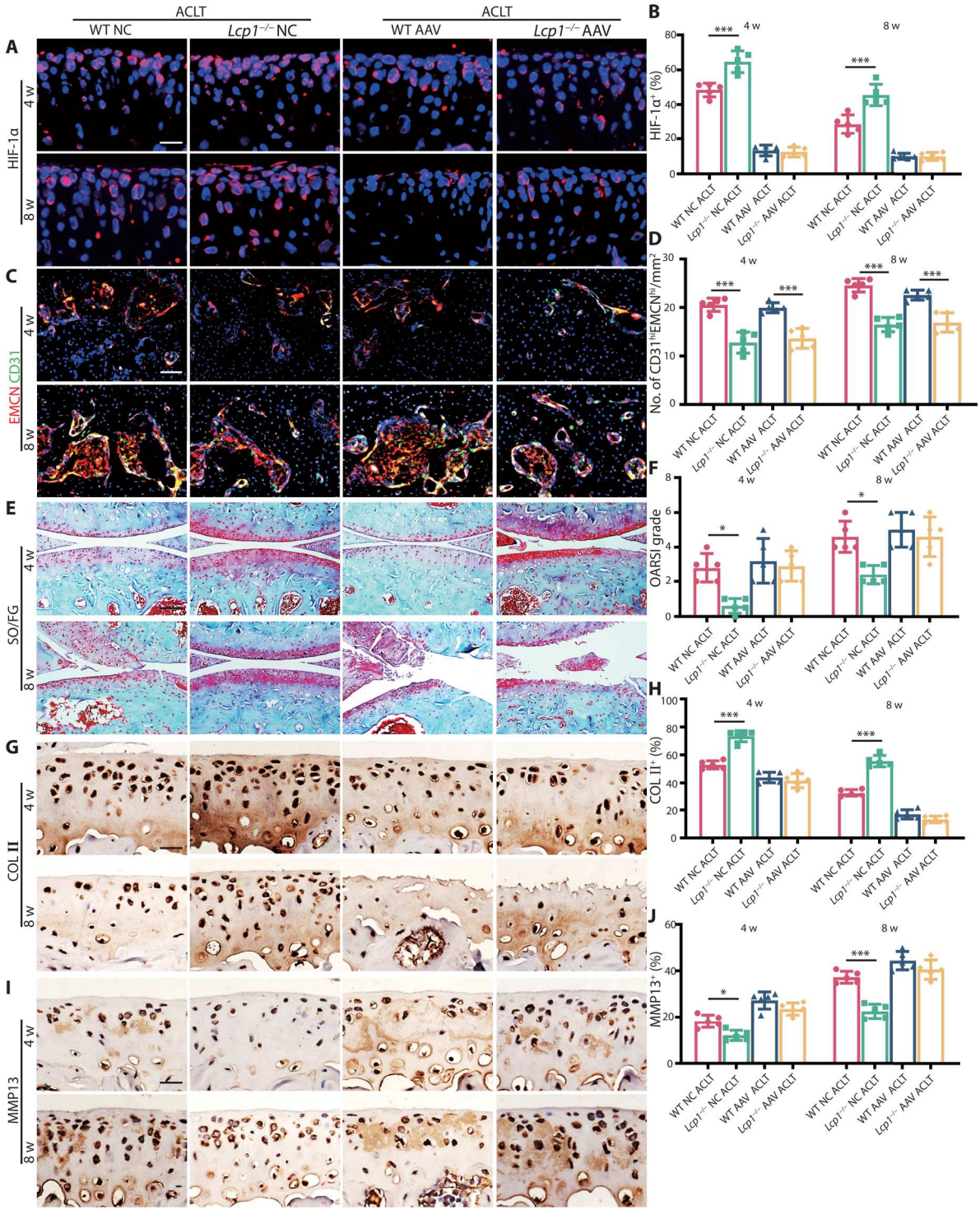

Fig. 5. Knockdown *Hif1a* in articular cartilage partially abolishes protective effect of *Lcp1* knockout. (**A**) Immunofluorescence staining of HIF-1α protein in tibial articular cartilage of *Lcp1*$^{-/-}$ and WT mice with *Hif1a* AAV or NC AAV at 4 and 8 weeks after ACLT. Scale bar, 20 μm. (**B**) Quantitative analysis of HIF-1α fluorescence intensity of mice articular cartilage. (**C**) Immunostaining of EMCN (red), CD31 (green), and Emcn^{hi}CD31^{hi} (yellow) cells in medial tibial subchondral bone of *Lcp1*$^{-/-}$ and WT mice with *Hif1a* AAV or NC AAV at 4 and 8 weeks after ACLT. Scale bar, 50 μm. (**D**) Quantification of CD31 and EMCN^{+} cells in subchondral bone marrow. (**E**) Knee articular cartilage Safranin O/Fast Green staining of *Lcp1*$^{-/-}$ and WT mice with *Hif1a* AAV or NC AAV at 4 and 8 weeks after ACLT. Scale bar, 100 μm. (**F**) OARSI grade of knee articular cartilage. (**G**) Representative images of COL II immunohistochemistry in articular cartilage of *Lcp1*$^{-/-}$ and WT mice with *Hif1a* AAV or NC at 4 and 8 weeks after ACLT. Scale bar, 20 μm. (**H**) Quantitative analysis of COL II^{+} area in articular cartilage. (**I**) Representative images of MMP13 immunohistochemistry in tibial articular cartilage of *Lcp1*$^{-/-}$ and WT mice with *Hif1a* AAV or NC at 4 and 8 weeks after ACLT. Scale bar, 20 μm. (**J**) Quantitative analysis of MMP13^{+} area in articular cartilage. $n = 5$ per group. *$P < 0.05$ and ***$P < 0.001$.

and *Lcp1*$^{-/-}$ mice (Fig. 5, E and F). The ratio of HC/CC decreased 1.2- and 1.6-fold in NC AAV WT mice at 4 and 8 weeks after ACLT compared with *Lcp1*$^{-/-}$ mice, but no significant difference was found between two groups after *Hif1a* knocked down (fig. S10, A and B). The area of COL II$^+$ region (Fig. 5, G and H) and ACAN$^+$ region (fig. S10, C and D) in NC AAC WT mice substantially decreased 14.1 to 23.0% compared to NC *Lcp1* knockout mice, while *Hif1a* knockdown decreased COL II and ACAN level in *Lcp1*$^{-/-}$ mice, and no significant difference was found compared to WT mice. The area of MMP13$^+$ region (Fig. 5, I and J), ADAMTS5$^+$ region (fig. S10, E and F), and COL X$^+$ region (fig. S10, G and H) in NC WT mice increased 1.46- to 1.78-fold compared to *Lcp1* knockout mice after ACLT. *Hif1a* silencing also increased the levels of those OA markers in *Lcp1* knockout mice, which indicated that the protective effect of *Lcp1* knockout was partially abolished in *Hif1a* AAV group. Besides the type-H vessel, we further checked whether *Hif1a* knockdown in cartilage had effects on subchondral bone structures. The micro-CT results showed that there was no significant difference of the bone volume or SBP.th between *Hif1a* AAV and NC in *Lcp1* knockout mice after ACLT, but the difference of BV/TV and Tb.pf between knockout mice and WT mice still existed (fig. S11, A to E). There was no statistical difference in the number of TRAP$^+$ cells in subchondral bone between two groups of *Lcp1* knockout mice, but few osteoclast cells were found in knockout mice at 4 weeks after ACLT (fig. S11, F and G). In addition, *Hif1a* knockdown in cartilage had little effect on the sensory nerve innervation in subchondral bone (fig. S11, H and I). Those results indicated that the *Hif1a* knockdown in cartilage did not affect subchondral bone changes.

To further confirm the role of HIF-1α in normal mice, we injected *Hif1a* AAV into WT and *Lcp1* knockout mice and performed sham operation. The *Hif1a* AAV could inhibit the expression of HIF-1α (fig. S12, A and B). However, the OARSI grade showed no significant difference between WT and *Lcp1* knockout mice at 4 and 8 weeks after sham operation (fig. S12, C and D). *Hif1a* AAV showed no significant effect on the ratio of HC/CC in WT and *Lcp1* knockout mice at 4 and 8 weeks after sham operation (fig. S13, A and B). The area of COL II$^+$ region (fig. S12, E and F), ACAN$^+$ region (fig. S13, C and D), MMP13$^+$ region (fig. S12, G and H), ADAMTS5 $^+$ region (fig. S13, E and F), and COL X$^+$ region (fig. S13, G and H) showed no difference between WT and *Lcp1* knockout mice after sham surgery, indicating that the knockdown of *Hif1a* in sham mice had no effect on cartilage metabolism. To sum up, silencing HIF-1α in cartilage abolishes the protective effects of OA progression by *Lcp1* knockout and exacerbates OA progression in WT mice, indicating that inhibiting subchondral bone remodeling alleviates cartilage degeneration through maintaining HIF-1α functions in chondrocytes.

Stabilizing HIF-1α protects articular cartilage in OA

As HIF-1α deficiency worsens OA progression, we speculated that stabilizing HIF-1α could have therapeutic effects on OA. We first confirmed that dimethyloxallyl glycine (DMOG) could preserve 49 to 74% of HIF-1α in ACLT mice at 4 and 8 weeks (Fig. 6, A and B). There were no significant difference of type-H vessel formation in subchondral bone between vehicle and DMOG group (Fig. 6, C and D). After intraperitoneal injection of DMOG, the OARSI grade substantially decreased 1.6- and 2.1-fold compared to the vehicle group at 4 and 8 weeks after ACLT (Fig. 6, E and F). The ratio of HC/CC increased 1.2- and 1.9-fold in DMOG treatment mice at 4 and 8 weeks compared to the vehicle group after ACLT (fig. S14, A and B). Also, the area of COL II$^+$ region (Fig. 6, G and H) and ACAN$^+$ region (fig. S14, C and D) in DMOG group substantially increased 2.6 to 18.1% compared to the vehicle group, and the area of MMP13$^+$ region (Fig. 6, I and J), ADAMTS5$^+$ region (fig. S14, E and F), and COL X$^+$ region (fig. S14, G and H) decreased 4.7 to 34.7% compared to vehicle mice after operation.

Next, we explored whether DMOG had effects on subchondral bone. The results of micro-CT revealed that there was no significant difference of the bone volume or SBP.th between DMOG and vehicle mice (fig. S15, A to E). There was no statistical difference of the number of TRAP$^+$ cells in subchondral bone between DMOG and vehicle mice with an average of 7.6 and 8 cells/mm^2 at 4 weeks after ACLT (fig. S15, F and G). Besides, the sensory nerve innervation of subchondral bone was not affected by intraarticular administration of DMOG (fig. S15, H and I), indicating that DMOG had no effects on abnormal bone remodeling in subchondral bone. Above all, stabilizing HIF-1α in chondrocytes directly could prevent cartilage degeneration in OA regardless of subchondral bone alterations.

Oroxylin A alleviates OA progression in WT mice

As *Lcp1* knockout could inhibit OA progression, we then explored whether LPL could serve as a target for OA treatment. Previously, we found that Oroxylin A (Oxy A) was a specific agent targeting LPL and could inhibit osteoclast formation (*16*). We checked whether Oxy A could retard the abnormal subchondral bone remodeling in OA. The results of micro-CT revealed that the bone volume and SBP.th increased at 2 and 4 weeks after ACLT between Oxy A and vehicle mice (Fig. 7, A and F to I). The number of TRAP$^+$ cells in subchondral bone after Oxy A treatment was 44.8 and 57.1% of vehicle group at 4 and 8 weeks after ACLT (Fig. 7, B and J). Then, we checked whether Oxy A could alleviate OA. After Oxy A treatment, the OARSI grade decreased 1.5- and 2.5-fold compared to the vehicle group at 4 and 8 weeks after ACLT (Fig. 7, C and K). The ratio of HC/CC increased 1.3- and 1.7-fold in Oxy A treatment mice at 4 and 8 weeks compared to the vehicle group after ACLT (fig. S16, A and E). In addition, the areas of COL II$^+$ region (Fig. 6, B and E) and ACAN$^+$ region (fig. S16, B and F) in Oxy A group were improved 11.8 to 57.3% compared to the vehicle group. The area of MMP13$^+$ region (Fig. 7, C and F), ADAMTS5$^+$ region (fig. S16, C and G), and COL X$^+$ region (fig. S16, D and H) decreased 4.9 to 37.0% compared to vehicle mice after operation. Next, we explored whether Oxy A had effects on subchondral bone. We evaluated the effects of Oxy A on sensory innervation and pain. The results showed that the level of NETRIN-1 increased at 2 weeks after ACLT in vehicle mice, and Oxy A decreased 1.2-fold of the expression of NETRIN-1 at same time (fig. S16, I and K). Consequently, the number of CGRP$^+$ nerve fibers decreased 1.3- and 1.4-fold in Oxy A mice compared to the vehicle (fig. S16, J and L). The von Frey test showed that the threshold of paw withdrawal was higher in Oxy A mice than vehicle mice from 4 to 7 weeks (fig. S16M). Above all, targeting LPL is a promising manner to protect subchondral bone and cartilage in OA.

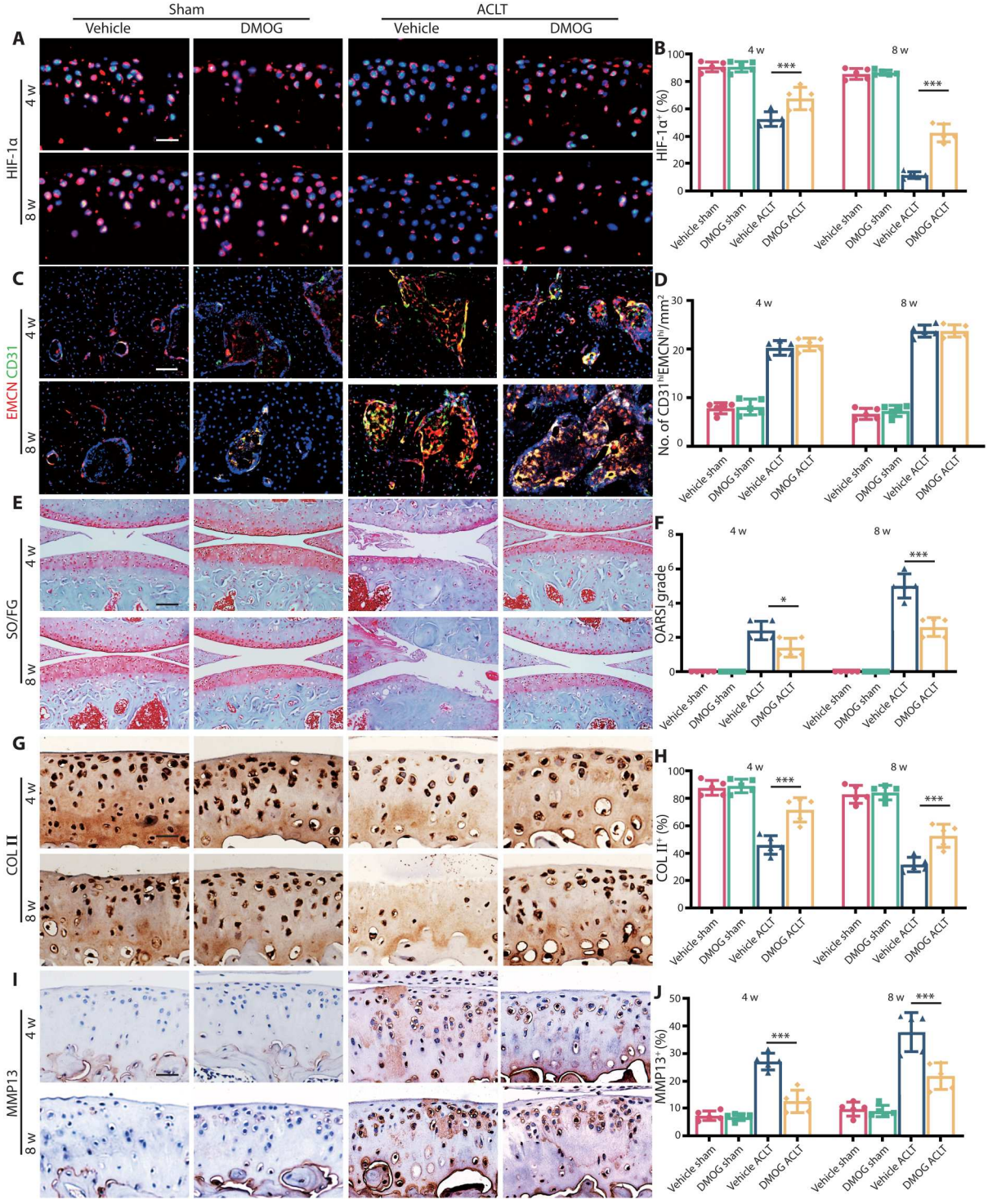

Fig. 6. HIF-1α stabilizer DMOG protects articular cartilage in OA. (**A**) Immunofluorescence staining of HIF-1α protein in tibial articular cartilage of WT mice with DMOG or normal saline at 4 and 8 weeks after ACLT. Scale bar, 20 μm. (**B**) Quantitative analysis of HIF-1α fluorescence intensity of mice articular cartilage. (**C**) Immunostaining of EMCN (red), CD31 (green), and Emcn^{hi}CD31^{hi} (yellow) cells in medial tibial subchondral bone of WT mice with DMOG or normal saline at 4 and 8 weeks after ACLT. Scale bar, 50 μm. (**D**) Quantification of CD31 and EMCN^{+} cells in subchondral bone marrow. (**E**) Knee articular cartilage Safranin O/Fast Green staining of WT mice with DMOG or normal saline at 4 and 8 weeks after ACLT. Scale bar, 100 μm. (**F**) OARSI grade of knee articular cartilage. (**G**) Representative images of COL II immunohistochemistry in articular cartilage of WT mice with DMOG or normal saline at 4 and 8 weeks after ACLT. Scale bar, 20 μm. (**H**) Quantitative analysis of COL II^{+} area in articular cartilage. (**I**) Representative images of MMP13 immunohistochemistry in tibial articular cartilage of WT mice with DMOG or normal saline at 4 and 8 weeks after ACLT. Scale bar, 20 μm. (**J**) Quantitative analysis of MMP13^{+} area in articular cartilage. $n = 5$ per group. *$P < 0.05$ and ***$P < 0.001$.

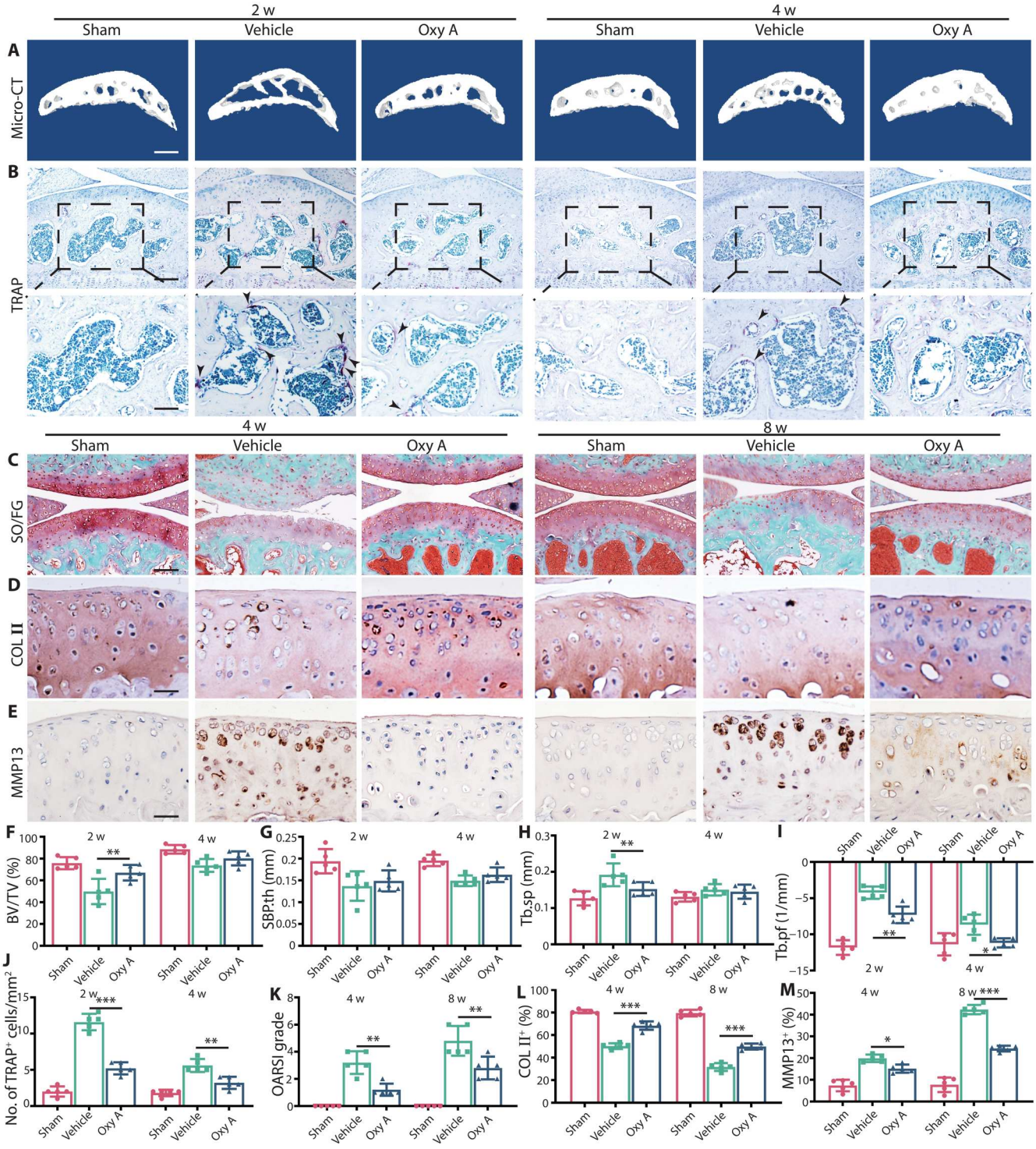

Fig. 7. Oxy A alleviates OA progression in WT mice. (**A**) Representative micro-CT 3D images of tibia subchondral bone of WT mice with Oxy A or normal saline at 2 and 4 weeks after ACLT. Scale bar, 500 μm. (**B**) TRAP staining images of tibial subchondral bone of WT mice with Oxy A or normal saline at 2 and 4 weeks after ACLT. Scale bar, 100 (top) and 50 μm (bottom). (**C**) Knee articular cartilage Safranin O/Fast Green staining of WT mice with Oxy A or normal saline. Scale bar, 100 μm. (**D**) Representative images of COL II immunohistochemistry in tibial articular cartilage of WT mice with Oxy A or normal saline at 4 and 8 weeks after ACLT. Scale bar, 20 μm. (**E**) Representative images of MMP13 immunohistochemistry in tibial articular cartilage of WT mice with Oxy A or normal saline at 4 and 8 weeks after ACLT. Scale bar, 20 μm. (**F** to **I**) Micro-CT quantitative analysis of tibial subchondral bone: BV/TV (%) (F), SBP.th (mm) (G), Tb.sp. (mm) (H), and Tb.pf (1/mm) (I). (**J**) Quantitative analysis of $TRAP^+$ cells in subchondral bone. (**K**) OARSI grade of knee articular cartilage. (**L**) Quantitative analysis of COL II^+ area in articular cartilage. (**M**) Quantitative analysis of $MMP13^+$ area in articular cartilage. $n = 5$ per group. $^*P < 0.05$, $^{**}P < 0.01$, and $^{***}P < 0.001$.

DISCUSSION

Subchondral bone and cartilage are tightly integrated to form osteochondral units, and the relationship between subchondral bone destruction and cartilage degeneration has always been a controversial issue (*21*). Under physiological conditions, subchondral bone maintains a low bone turnover rate and stable microstructure to bear joint load through strictly inhibiting osteoclast formation (*22*). In early OA, abnormal biomechanical and biochemical factors recruit and promote osteoclast differentiation, which results in enhanced bone turnover rate with subchondral bone plate thinning and trabecular bone thickness decreasing (*23*). Conversely, the late OA shows subchondral bone sclerosis characterized by subchondral bone plate and trabecular bone thickening due to excess bone formation (*24*). It is very mysterious and intriguing that the osteoclast shows and disappears, but the cartilage continuously undergoes degeneration. On the basis of the above, we first hypothesized that osteoclasts introduced certain factors that contribute to sustained cartilage deterioration even without osteoclasts.

Studies showed that targeting abnormal activation of osteoclast could block abnormal subchondral bone remodeling in the very beginning and protect articular cartilage degeneration (*25*–*27*). In vitro and animal experiments showed that the blockage of osteoclast by bisphosphonates significantly alleviated OA progression (*28*). Clinical studies, however, provided conflicting conclusions (*29*). Several retrospective studies have found that the incidence of OA in patients with osteoporosis using bisphosphonates is low, and the use of bisphosphonates can modify OA, while some prospective studies show that the therapeutic effect of bisphosphonates on OA is uncertain (*28*, *29*). Besides the fact that the classification of OA is not clear, a reasonable explanation of this heterogeneity is the difference in the disease stages of treatment initiation. Osteoclasts showed transiently in the initial stage of OA. Blockade of osteoclasts can treat OA, but the patient should be in the stage of osteoclast activation. Therefore, it is of vital significance to explore the mechanism of OA progression after transient activation of osteoclasts.

Previously, we reported that LPL, an actin-bundling protein, is indispensable for osteoclast fusion and resorption (*16*). In this study, we first used *Lcp1* knockout mice and performed ACLT to observe whether *Lcp1* knockout could prevent OA progression. Although *Lcp1* knockout increased bone volume in bone marrow cavity, it did not affect subchondral bone due to the very low bone turnover rate. To exclude the possible interference of chondrocytes, we showed that LPL was not expressed by chondrocytes. As previously reported, retarding osteoclastogenesis in subchondral bone inhibited the bone turnover rate in early stage of OA and protected the cartilage from degeneration.

How osteoclasts initiate cartilage degeneration is still unclear. In early OA, subchondral bone shows increased bone resorption, but in advanced OA, it shows abnormal bone formation, which is closely correlated to cartilage degeneration, similar to endochondral ossification (*30*). Hu *et al.* (*31*) proposed the conception of "osteoclast (OC)-chondrocyte (CC) cross-talk" and described several pathways by which these cells might communicate: (i) OC and CC interact via secreted cytokines crossing micro-splits and vessels. (ii) OC precursors could migrate to the cartilage by invasive vascularization. (iii) Mature OC moves into subchondral bone and overlying cartilage and interplays with CC in the cartilage area. (iv) Subchondral bone deterioration mediated by OC transfers shear forces to the cartilage and subsequently results in aberrant chondrocyte metabolism (*31*). As the type-H vessel couples bone resorption and formation (*32*), we considered that subchondral bone type-H vessels could link osteoclasts, osteoblasts, and articular chondrocytes.

The type-H vessel, which is rare in normal subchondral bone, is notably increased in OA induced by osteoclasts (*19*, *33*). Type-H vessels not only bring secreted mediators and mononuclear cells but also introduce abundant oxygen, an important small molecule in cartilage homeostasis. Normally, the subchondral bone and cartilage are very hypoxic. The level of oxygen is 1 to 5% in cartilage and 7% in subchondral bone (*18*). Several invasive tests of subchondral bone local pO_2 based on mass spectrometry reported various value of pO_2 from 30 to 39 mmHg (*34*, *35*). However, using oxygen electrode assessment was deficient in spatial resolution, and the implant of the needle electrode may destroy the microvasculature. A direct in vivo measurement of pO_2 using two-photon phosphorescence lifetime microscopy reported the pO_2 in bone marrow, but the data of subchondral bone were absent (*36*). Thus, we determined the pO_2 of subchondral bone with a noninvasive and in vivo hypoxia probe.

In this study, we used ^{18}F-FMISO as a hypoxia probe and detected the hypoxia status of subchondral bone and cartilage through PET-CT in vivo. ^{18}F-FMISO based on the nitroimidazole structure is the first hypoxia PET tracer used in clinical studies (*37*). ^{18}F-FMISO is reduced and covalently bound to intracellular macromolecules in hypoxic cells and will not escape from those cells (*38*). Its binding is inversely proportional to the level of oxygen and substantial retention occurs in tissue where oxygen levels below 10 mmHg. We found that in early stage of OA, uptake of ^{18}F-FMISO decreased, and the pressure of O_2 increased in the ACLT joint. Pimonidazole immunostaining further confirmed the results that pO_2 increased in early stage of OA. Combining with the results of increased type-H vessels in OA, we believed that type-H vessels induced by osteoclasts altered the hypoxia environment of subchondral bone and cartilage.

Then, we explored how increased oxygen affected chondrocyte degeneration. In recent years, HIF-1α has been recognized as a protective factor in maintaining normal chondrocyte function, mainly through promoting chondrocyte metabolism, differentiation, and matrix secretion (*39*–*41*). HIF-1α serves as a pivotal factor for chondrocytes by maintaining anaerobic glycolysis and impeding apoptosis via mitophagy (*42*, *43*). HIF-1α is also a positive regulator for the expression of SRY-Box Transcription Factor 9 (SOX9), COL2A1, and ACAN and inhibits the expression of COL1A1, COL1A2, COL10A1, and MMP13 to promote chondrocyte differentiation and matrix synthesis (*40*, *44*–*46*).

According to our results, we found that the level of HIF-1α in chondrocyte was negatively correlated with the severity of OA. To further explore the roles of HIF-1α in OA, we reanalyzed the single-cell RNA-seq data of OA human chondrocytes (GSE104782) (*20*). We focused on HTCs, a group of cells involved in endochondral ossification and CC duplication in OA progression. We found that HTCs had two different subgroups. A subgroup of HTCs, which expressed high levels of *MMP13*, *RUNX2*, *COL1A1*, and *COL10A1*, was termed OA-associated HTC. KEGG and GO enrichment analysis indicated that OA-associated HTC were involved in endochondral ossification, ossification replacement, and endochondral bone morphogenesis, while another subgroup of HTCs was named regulatory HTC, involved in regulation of calcium channel activity,

AMPA receptor activity, and circadian sleep-wake cycle. The immunofluorescence results confirmed the presence of OA-associated HTC and showed that these cells were mainly found in severe OA cartilage. GSVA results showed that the HIF-1α activation was negatively correlated with OA pathway activation in OA-HTC.

In our study, we found that the degradation of HIF-1α played a key role in cartilage degeneration in OA. Stabilization of HIF-1α could prevent OA progression. We used *Hif1a* knockdown AAV and HIF-1α stabilizer DMOG in *Lcp1* knockout and WT OA mice to verify that HIF-1α can influence articular cartilage independently from subchondral bone alteration. Although *Lcp1* knockout reduced the bone remodeling in subchondral bone, silencing HIF-1α mediated by *Hif1a* AAV could still cause articular cartilage degeneration and abolish the protective effect in $Lcp1^{-/-}$ ACLT mice. On the other hand, although subchondral bone remodeling was not inhibited in WT ACLT mice, DMOG stabilized HIF-1α and retarded OA progression in a nonhypoxic environment, consistent with a previous study by Hu *et al.* (*39*). We also evaluated the effects of HIF-1α knockdown or stabilization in cartilage on subchondral bone. Results showed that HIF-1α knockdown or stabilization did not have a significant impact on subchondral bone remodeling, type-H vessel formation, or sensory nerve innervation. HIF-1α could be a potential target in preventing cartilage degeneration in OA.

The results presented in our study further supported that inhibition of osteoclasts can modify OA. Our study gives an answer to the roles of osteoclasts in OA onset and progression. Abnormal load leads to the activation of osteoclasts and causes bone resorption, angiogenesis, and sensory nerve innervation. Vascular invasion leads to the invasion of oxygen-rich type-H vessels into the subchondral bone, disrupting the hypoxic environment throughout the joint (Fig. 8). Therefore, the stage of OA intervention is important. In the early stage, blocking osteoclasts could help delay OA progression. This is the window for the administration of anti-osteoclast agents. At the developing stage of OA, the usage of anti-osteoclast agents could not reverse the formation of H-type vessels, the disrupted hypoxia condition. Therefore, OA continues to deteriorate. At this time, maintaining hypoxic environment in cartilage and stabilizing HIF-1α in chondrocytes could help delay the OA progression regardless of subchondral bone changes.

Some limitations of this study should be addressed. First, we unveiled the role of HIF-1α stabilizer in OA treatment in rodents. However, its therapeutic effect in human should be further explored. Besides, systemic administration of HIF-1α stabilizer may lead to off-target effect. Local injection with suitable drug delivery system would further improve the outcomes. Second, the definitive conclusion that osteoclasts directly induce the increase of oxygen levels needs further studies. The clinical significance of stabilizing articular HIF-1α needs verification by human trials. Last, Oxy A is hydrophobic small molecule that decreases the bioavailability via systematic administration. Several biological materials including hydrogels, nanozyme, and nanoparticle has been reported as promising carriers (*47*–*50*). Thus, we have developed a long-stranded, cartilage-targeted, and enzyme-responded biological materials that contain a DMOG to improve the therapeutic effects on cartilage protection in further study.

The highlights of this study are as follow: In subchondral bone, type H vessels induced by osteoclasts in early OA elevate pO_2 levels. (i) Increased pO_2 levels abolish HIF-1α functions of maintaining chondrocytes homeostasis; and (ii) a subgroup of HTCs with decreased HIF-1α activity is highly associated with OA progression.

MATERIALS AND METHODS

Study design

This study was performed to explore the roles and mechanisms of osteoclasts in subchondral bone area in cartilage degeneration in OA. First, we used *Lcp1* knockout mice with inhibited osteoclastogenesis in subchondral bone to establish ACLT OA model. We compared the difference of cartilage degeneration, subchondral bone remodeling, angiogenesis, and hypoxia environment change in subchondral bone between *Lcp1* knockout mice and WT mice in ACLT model through immunofluorescence and histomorphometric analyses. ^{18}F-FMISO PET/CT analysis was used to detect hypoxic environment of knee joint in vivo at different times after ACLT. The vital role of HIF-1α in maintaining chondrocyte stability and preventing hypertrophy was verified by single-cell RNA-seq. *Hif1a* knockdown AAV and HIF-1α stabilizer were used to confirm that *Lcp1* knockout protected cartilage through stabilizing HIF-1α in chondrocytes. Potentiality of LPL as a therapeutic target of OA was testified by systematic administration of Oxy A, which was proved as an LPL-specific inhibitor in our former study. Samples were randomly assigned into distinct intervention groups, and littermates were included in the control group. Five samples were used for statistical analysis in each experiment. The study was approved by Shanghai Model Organisms [SCXK (Shanghai) 2017-0010 and SYXK (Shanghai) 2017-0012], and Institutional Animal Care and Use Committee guidelines were followed for animal experiments.

Mouse models

Lcp1 knockout mice on C57BL/6 background were created by the Shanghai Model Organisms in our former study (*16*). Male C57 mice (8 weeks old) were obtained from Weitonglihua Corporation (Beijing, China). The rodent researches were carried out in the pathogen-free environment. Laboratory conditions for mice were listed below: temperature, 22°C; humidity, 50%; light-dark cycle, 12 hours; water and food, available. In line with our previous protocol, ACLT surgery was performed to generate OA mouse model. Briefly, after anesthesia with pentobarbital sodium, a longitudinal cutaneous incision was made at medial side of the right knee. The ACL was transected after open knee joint through medial approach of ligamentum patellae under a surgical microscope. The rodents were randomly divided into different groups: Sham (performed the incision without ACL transection), ACLT, groups of different intervention (ACLT mice intraarticularly injected with *Hif1a* AAV and DMOG or Oxy A intraperitoneally), and vehicle (ACLT mice injected with saline).

Human samples

Human samples of medial tibia plateau were collected during total knee arthroplasty operations. Subchondral bone and articular cartilage samples were cut into 1- to 2-cm pieces, fixed in 4% paraformaldehyde (PFA) solution (G1101-500ML Servicebio, Wuhan, China) for 2 days, and decalcified in 10% EDTA (G1105-500ML, Servicebio, Wuhan, China) for 6 months. Samples were embedded in paraffins or optimal cutting temperature (OCT) compound and cut into 5-μm sections. The experiments were approved by the ethics committee of Shanghai University, no. ECSHU 2021-146.

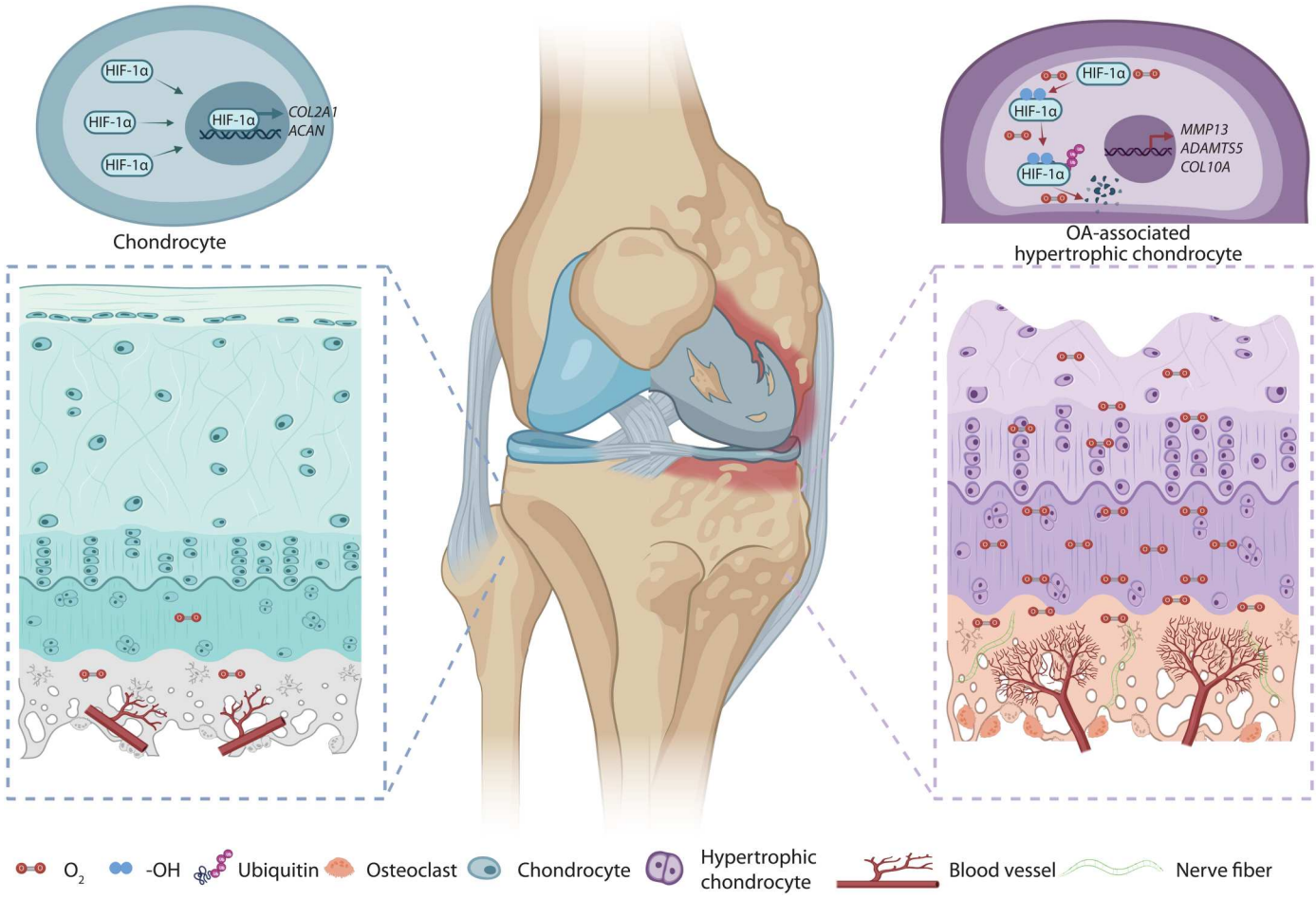

Fig. 8. Oxygen from the subchondral bone leads to cartilage degeneration. Hypoxic environment is altered by type-H vessels recruited by osteoclasts and high-level oxygen contributes to cartilage degeneration by degrading HIF-1α. Created by Biorender.

We informed the patient before the surgery that the medial tibia plateau would be used as a sample for scientific research. The patients expressed their willingness to participate and signed the informed consent form.

Lcp1 knockout verification

The mouse tail was and placed into the centrifuge tube. Lysis solution and proteinase K stock solution (provided by the Shanghai Model Organisms) were added into the tube, and the tubes were placed in a hybridization oven and rotated at 56°C overnight. After centrifugation, absolute ethanol was added into the supernatant. After centrifuging the sample, the precipitate was collected, and 70% ethanol was added. The sample was centrifuged again, and sterilized water was added into the precipitate at room temperature. After the complete dissolution of DNA, standard polymerase chain reaction (PCR) experiments were performed as previously described (*16*). The primer used are as follows: P1, (forward: 5′-CAGGAGACCTCAAAGCCAACC-3′), P2 (reverse: 5′-GCGTCCATTAAGGCTGCTCC-3′), and P3 (forward: 5′-GGGGTTGTAGAGTCGATATTTGCT-3′).

For the mRNA level of *Lcp1* in the spleen, lung, and thymus, the tissue (50 mg) was added into TransZol Up solution and homogenized with a tissue homogenizer for 2 min. Next, standard quantitative PCR was performed as previously described (*16*). The *Lcp1* primers are as follows: P1 (forward: 5′-AGGTTGCCAAAACCTTCCGA-3′) and P2 (reverse: 5′-TCAATGTCAGCAAACAACCCA-3′).

Hif1a knockdown AAV construction

Recombinant AAV virus was constructed by transferring knockdown vector and auxiliary plasmids to AAV-293 cells. The AAV virus was produced and purified according to standard protocol, and the OBIO Technology (Shanghai, China) provided support in AAV construction. A scramble DNA sequence was cloned into AAV plasmid as control. To knockdown *Hif1a* in vivo, designed *Hif1a*-shRNA sequences were cloned into pAAV-U6-shRNA-CMV-EGFP-WPRE plasmid. AAV-sh*Hif1a* virus was obtained by co-transferring the constructed plasmids and auxiliary plasmids into AAV-293 cells and purified with a standard protocol. The purified virus was diluted in sterile PBS. *Hif1a* knockdown shRNA sequence is 5′-GUGGAUAGCGAUAUGGUCAUU-3′ (*51*).

^{18}F-FMISO PETCT analyses

^{18}F-FMISO was synthetized as stated by the means proposed by Yu and He (*38*, *52*). The 1-(2-nitro-1′- imidazolyl)-2-*O*-tetrahydropyranyl-3-*O*-toluenesulfonylpropanediol precursor was obtained from

ABX GmbH (Radeberg, Germany), and ^{18}fluoride was got from BV Cyclotron VU (Amsterdam, Netherlands). Radio synthesis was completed in an automated synthesizer. Male mice of the same age were intravenously injected with 100 MBq of ^{18}F-FMISO in 0.2 ml of normal saline. Mice were detected in PET/CT 1 hour after the injection of ^{18}F-FMISO. Images were collected and analyzed by Bee DICOM Viewer.

Micro-CT analyses

Tibia subchondral bone vasculature was evaluated by Micro-CT as reported earlier (*53*). Mice were anesthetized with pentobarbital sodium. The tibia subchondral bone vessels were washed with normal saline solution, 4% PFA solution, and normal saline solution through heart in proper sequence. Then, the intravascular contrast medium (MICROFIL, MV-120, Flow Tech) was injected. The mice were preserved at 4°C for 12 hours before the knee joints were harvested. The knee joints were fixed for 3 days in 4% PFA and decalcified in 10% EDTA for 21 days before scan. The vascular volume in subchondral bone was analyzed. The region of interest was central of medial tibia plateau. The BV/TV, SBP.th, Tb.sp, and Tb.pf were calculated with CTAn, and the 3D reconstruction of joint was performed with CTVol.

Microangiography

Tibia subchondral bone vasculature was evaluated by micro-CT as reported earlier (*25*). Mice were anesthetized with pentobarbital sodium. The tibia subchondral bone vessels were washed with normal saline solution, 4% PFA solution, and normal saline solution through heart in proper sequence. Then, the intravascular contrast medium (MICROFIL, MV-120, Flow Tech) was injected. The mice were preserved at 4°C for 12 hours before the knee joints were harvested. The knee joints were fixed for 3 days in 4% PFA and decalcified in 10% EDTA for 21 days prior before scan. The vascular volume in subchondral bone was analyzed. The region of interest was central of medial tibia plateau.

Histological analysis

Knee joints were collected, fixed in 4% PFA for 2 days, and decalcified in 10% EDTA for 14 days. Next, the joints were embedded in paraffin or OCT and serially sectioned at 5 μm in the sagittal plane of the central medial compartment of the joints (*54*). Then, hematoxylin and eosin (H&E; G1005-500ML, Servicebio, Wuhan, China), Safranin O and fast green (G1053-100ML Servicebio, Wuhan, China), and TRAP staining (G1050-50T, Servicebio, Wuhan, China) were done according to regular procedures (*16*, *25*). A light microscope (Olympus BX53 and Nikon ECLIPSE Ci-L plus) was used for imaging. The tidemark line labeled the bound between HC and CC. H&E staining image was used to evaluate the thickness of HC and CC. The OARSI grade was used to analyze the degradation of tibial plateau cartilage (*55*). The TRAP staining was used to count osteoclasts in subchondral bone (*5*).

Immunofluorescence and histomorphometry

Antibodies against ACAN (1:500; Servicebio, GB11373) and COL II (1:500; Servicebio, GB11021) were obtained from Servicebio (Wuhan, China). MMP13 (1:200; Proteintech, 18165-1-AP), CHDH (1:200; Proteintech, 17356-1-AP), CTTNBP2 (1:100; Proteintech, 17893-1-AP), PRKG2 (1:100; Proteintech, 55138-1-AP), and WNT5A (1:200; Proteintech, 55184-1-AP) were purchased from Proteintech (Wuhan, China). LPL (1:200; Thermo Fisher Scientific, PA5-85216) and ADAMTS5 (1:500; Thermo Fisher Scientific, PA5-27165) were obtained from Thermo Fisher Scientific (Waltham, USA). Collagen Type X (COLX)(1:500; Abcam, ab260040), CD31 (1:200; Abcam, ab182981), and CGRP (1:200; Abcam, ab36001) were obtained from Abcam (Cambridge, UK). EMCN (1:50; Santa Cruz Biotechnology, sc-65495) was obtained from Santa Cruz Biotechnology (Dallas, USA). HIF-1α (1:50; Novus, NB100-105), tartrate-resistant acid phosphatase (TRACP) (1:100; Novus, NBP2-45294), and NETRIN-1 (1:100; Novus, NB100-1605) were purchased from Novus (Littleton, USA). Paraffin sections were dewaxed in dimethylbenzene for 10 min twice, and dehydration was performed in 100, 100, 95, 80, and 75% ethanol for 5 min each time. Antigen retrieval was performed in EDTA (pH 9.0) or citrate (pH 6.0) at 95°C for 20 min. Until sections cooled down to room temperature, 3% H_2O_2 was used to block peroxidase for 15 min. Goat serum (10%) was used to block sections for 1 hour. Primary antibody were diluted into appropriate concentration according to instructions and incubated for 12 hours at 4°C. After primary antibody was washed three times, horseradish peroxidase–conjugated secondary antibody or fluorescein-conjugated secondary antibody was incubated for 30 to 60 min at room temperature according to the manual. Diaminobenzidine (DAB) kit and hematoxylin were used in immunochemistry staining. 4′,6-Diamidino-2-phenylindole was used to stain nucleus in immunofluorescence. The light microscopes (Olympus BX53 and Nikon ECLIPSE Ci-L plus) were used for section imaging. The number of positive cells or area in sections was quantified using ImageJ (*56*).

Hypoxia probe detection

Hypoxyprobe green kit (Hypoxyprobe, Inc., HP6-100) was purchased from Hypoxyprobe. Pimonidazole (60 mg/kg) was intraperitoneally injected into mice 1 hour before euthanizing. Paraffin sections were prepared as described above. Primary antibody conjugated with fluorescein isothiocyanate in kit was used to detect pimonidazole at 1:100 dilution.

Single-cell RNA-seq data analyses

We downloaded single-cell RNA-seq data from NCBI (GSE10478) and processed the unique molecular identifier count matrix with the R package Seurat (version 3.1.1) (*57*). A total of 1600 cells were obtained for following evaluation. Library size normalization was done using Normalize Data function in Seurat to acquire normalized number.

Top variable genes were verified by the means reported by Macosko *et al.* (*58*). The most variable genes were collected using Find Variable Genes function in Seurat. Principal components analysis (PCA) was done to depress the dimensionality with RunPCA function in Seurat (*57*). To cluster cells, graph-based clustering was done on the basis of each cell gene expression profile via the Find Clusters function. Visualization of cells was done by a two-dimensional *t*-distributed stochastic neighbor embedding (t-SNE) algorithm using the RunTSNE function in Seurat. Find All Markers function was used to verify marker genes of each cluster. Find All Markers function determined positive markers compared to other cells.

Differentially expressed genes (DEGs) were established via the Find Markers function in Seurat. Significant DEGs threshold were P value of <0.05 and $|\log_2$ fold change$| > 0.5$. GO enrichment and

KEGG pathway enrichment analysis of DEGs were respectively carried out by R based on the hypergeometric distribution.

Von Frey tests

Von Frey filaments (touch test, USA) were used to measure the 50% paw withdrawal threshold (50% PWT) as our previous study. Briefly, mice were put into cages for 30 min to adapt. Von Frey hairs with different forces (0.04, 0.07, 0.16, 0.4, 0.6, 1.0, 1.4, and 2.0 g) were used in this test, and 2.0 g was served as the cutoff threshold. Mechanical allodynia was analyzed on the basis of the up-down theory from Dixon and was performed each week (*59*). The filament was stabbed under the middle plantar area of the right hind paw. Negative response record as "o," and higher force was used in next test. Positive response record as "x," and next lower force was used. When the difference of response occurred ("ox" or "xo"), four more experiments were done to get six results. The interval between neighboring stab was 6 min. 50% PWT was analyzed by the formula: $10[Xf + k\delta] / 10^4$, where Xf is the value of the last force applied, δ is a constant of serial force, and k is derived from response pattern.

Statistical analyses

All data were presented as the means ± SD or SEM. Comparisons between two groups were performed by the two-tailed Student's t test. Comparisons among multiple groups were analyzed by the one-way analysis of variance (ANOVA). The results were visualized and analyzed by the GraphPad PRISM software, and a $P < 0.05$ implied that differences were statistically significant.

Supplementary Materials

This PDF file includes:
Figs. S1 to S16
Legends for movies S1 and S2

Other Supplementary Material for this manuscript includes the following:
Movies S1 to S2

View/request a protocol for this paper from *Bio-protocol*.

REFERENCES AND NOTES

1. J. N. Katz, K. R. Arant, R. F. Loeser, Diagnosis and treatment of hip and knee osteoarthritis: A review. *JAMA* **325**, 568–578 (2021).
2. D. J. Hunter, S. Bierma-Zeinstra, Osteoarthritis. *Lancet* **393**, 1745–1759 (2019).
3. A. Latourte, M. Kloppenburg, P. Richette, Emerging pharmaceutical therapies for osteoarthritis. *Nat. Rev. Rheumatol.* **16**, 673–688 (2020).
4. L. A. Holzer, M. Kraiger, E. Talakic, G. A. Fritz, A. Avian, A. Hofmeister, A. Leithner, G. Holzer, Microstructural analysis of subchondral bone in knee osteoarthritis. *Osteoporosis Int.* **31**, 2037–2045 (2020).
5. Y. Hu, X. Chen, S. Wang, Y. Jing, J. Su, Subchondral bone microenvironment in osteoarthritis and pain. *Bone Res* **9**, 20 (2021).
6. C. K. Kwoh, Clinical relevance of bone marrow lesions in OA. *Nat. Rev. Rheumatol.* **9**, 7–8 (2013).
7. F. Zhou, X. Han, L. Wang, W. Zhang, J. Cui, Z. He, K. Xie, X. Jiang, J. Du, S. Ai, Q. Sun, H. Wu, Z. Yu, M. Yan, Associations of osteoclastogenesis and nerve growth in subchondral bone marrow lesions with clinical symptoms in knee osteoarthritis. *J. Orthop. Translat.* **32**, 69–76 (2022).
8. M. Huang, J. Zhao, Y. Huang, L. Dai, X. Zhang, Meta-analysis of urinary C-terminal telopeptide of type II collagen as a biomarker in osteoarthritis diagnosis. *J. Orthop. Transl.* **13**, 50–57 (2018).
9. G. Zhen, C. Wen, X. Jia, Y. Li, J. L. Crane, S. C. Mears, F. B. Askin, F. J. Frassica, W. Chang, J. Yao, J. A. Carrino, A. Cosgarea, D. Artemov, Q. Chen, Z. Zhao, X. Zhou, L. Riley, P. Sponseller, M. Wan, W. W. Lu, X. Cao, Inhibition of TGF-β signaling in mesenchymal stem cells of subchondral bone attenuates osteoarthritis. *Nat. Med.* **19**, 704–712 (2013).
10. H. Löfvall, H. Newbould, M. A. Karsdal, M. H. Dziegiel, J. Richter, K. Henriksen, C. S. Thudium, Osteoclasts degrade bone and cartilage knee joint compartments through different resorption processes. *Arthritis Res. Ther.* **20**, 67 (2018).
11. X. Chen, X. Zhi, J. Wang, J. Su, RANKL signaling in bone marrow mesenchymal stem cells negatively regulates osteoblastic bone formation. *Bone Res.* **6**, 34 (2018).
12. Y. Hu, X. Li, X. Zhi, W. Cong, B. Huang, H. Chen, Y. Wang, Y. Li, L. Wang, C. Fang, J. Guo, Y. Liu, J. Cui, L. Cao, W. Weng, Q. Zhou, S. Wang, X. Chen, J. Su, RANKL from bone marrow adipose lineage cells promotes osteoclast formation and bone loss. *EMBO Rep.* **22**, e52481 (2021).
13. W. Su, G. Liu, X. Liu, Y. Zhou, Q. Sun, G. Zhen, X. Wang, Y. Hu, P. Gao, S. Demehri, X. Cao, M. Wan, Angiogenesis stimulated by elevated PDGF-BB in subchondral bone contributes to osteoarthritis development. *JCI. Insight* **5**, e135446 (2020).
14. J. Fernández-Torres, G. A. Martínez-Nava, M. C. Gutiérrez-Ruíz, L. E. Gómez-Quiroz, M. Gutiérrez, Role of HIF-1α signaling pathway in osteoarthritis: A systematic review. *Rev. Bras. Reumatol. Engl. Ed.* **57**, 162–173 (2017).
15. C. Barranco, Osteoarthritis: Animal data show VEGF blocker inhibits post-traumatic OA. *Nat. Rev. Rheumatol.* **10**, 638 (2014).
16. X. Li, L. Wang, B. Huang, Y. Gu, Y. Luo, X. Zhi, Y. Hu, H. Zhang, Z. Gu, J. Cui, L. Cao, J. Guo, Y. Wang, Q. Zhou, H. Jiang, C. Fang, W. Weng, X. Chen, X. Chen, J. Su, Targeting actin-bundling protein L-plastin as an anabolic therapy for bone loss. *Sci. Adv.* **6**, eabb7135 (2020).
17. S. Zhu, J. Zhu, G. Zhen, Y. Hu, S. An, Y. Li, Q. Zheng, Z. Chen, Y. Yang, M. Wan, R. L. Skolasky, Y. Cao, T. Wu, B. Gao, M. Yang, M. Gao, J. Kuliwaba, S. Ni, L. Wang, C. Wu, D. Findlay, H. K. Eltzschig, H. W. Ouyang, J. Crane, F. Q. Zhou, Y. Guan, X. Dong, X. Cao, Subchondral bone osteoclasts induce sensory innervation and osteoarthritis pain. *J. Clin. Invest.* **129**, 1076–1093 (2019).
18. J. E. Lafont, Lack of oxygen in articular cartilage: Consequences for chondrocyte biology. *Int. J. Exp. Pathol.* **91**, 99–106 (2010).
19. Z. Cui, J. Crane, H. Xie, X. Jin, G. Zhen, C. Li, L. Xie, L. Wang, Q. Bian, T. Qiu, M. Wan, M. Xie, S. Ding, B. Yu, X. Cao, Halofuginone attenuates osteoarthritis by inhibition of TGF-β activity and H-type vessel formation in subchondral bone. *Ann. Rheum. Dis.* **75**, 1714–1721 (2016).
20. Q. Ji, Y. Zheng, G. Zhang, Y. Hu, X. Fan, Y. Hou, L. Wen, L. Li, Y. Xu, Y. Wang, F. Tang, Single-cell RNA-seq analysis reveals the progression of human osteoarthritis. *Ann. Rheum. Dis.* **78**, 100–110 (2018).
21. T. Hodgkinson, D. C. Kelly, C. M. Curtin, F. J. O'Brien, Mechanosignalling in cartilage: An emerging target for the treatment of osteoarthritis. *Nat. Rev. Rheumatol.* **18**, 67–84 (2022).
22. A. Bertuglia, M. Lacourt, C. Girard, G. Beauchamp, H. Richard, S. Laverty, Osteoclasts are recruited to the subchondral bone in naturally occurring post-traumatic equine carpal osteoarthritis and may contribute to cartilage degradation. *Osteoarthr. Cartilage* **24**, 555–566 (2016).
23. H. Fang, L. Huang, I. Welch, C. Norley, D. W. Holdsworth, F. Beier, D. Cai, Early changes of articular cartilage and subchondral bone in the DMM mouse model of osteoarthritis. *Sci. Rep.* **8**, 2855 (2018).
24. G. O. M. Azzini, G. S. Santos, S. B. C. Visoni, V. O. M. Azzini, R. G. D. Santos, S. C. Huber, J. F. Lana, Metabolic syndrome and subchondral bone alterations: The rise of osteoarthritis – A review. *J. Clin. Orthop. Trauma* **11**, S849–S855 (2020).
25. C. Fang, J. Guo, Y. Wang, X. Li, H. Zhang, J. Cui, Y. Hu, Y. Jing, X. Chen, J. Su, Diterbutyl phthalate attenuates osteoarthritis in ACLT mice via suppressing ERK/c-fos/NFATc1 pathway, and subsequently inhibiting subchondral osteoclast fusion. *Acta Pharmacol. Sin.* **43**, 1299–1310 (2022).
26. J. H. Duarte, Alendronate treatment improves pathology in animal model of OA by blocking osteoclastic bone resorption. *Nat. Rev. Rheumatol.* **10**, 446 (2014).
27. G. Cai, D. Aitken, L. L. Laslett, J. P. Pelletier, J. Martel-Pelletier, C. Hill, L. March, A. E. Wluka, Y. Wang, B. Antony, L. Blizzard, T. Winzenberg, F. Cicuttini, G. Jones, Effect of intravenous zoledronic acid on tibiofemoral cartilage volume among patients with knee osteoarthritis with bone marrow lesions: A randomized clinical trial. *JAMA* **323**, 1456–1466 (2020).
28. E. F. Eriksen, M. Shabestari, A. Ghouri, P. G. Conaghan, Bisphosphonates as a treatment modality in osteoarthritis. *Bone* **143**, 115352 (2021).
29. S. Fernandez-Martin, M. Lopez-Pena, F. Munoz, M. Permuy, A. Gonzalez-Cantalapiedra, Bisphosphonates as disease-modifying drugs in osteoarthritis preclinical studies: A systematic review from 2000 to 2020. *Arthritis Res. Ther.* **23**, 60 (2021).
30. S. R. Goldring, M. B. Goldring, Changes in the osteochondral unit during osteoarthritis: Structure, function and cartilage–Bone crosstalk. *Nat. Rev. Rheumatol.* **12**, 632–644 (2016).
31. W. Hu, Y. Chen, C. Dou, S. Dong, Microenvironment in subchondral bone: Predominant regulator for the treatment of osteoarthritis. *Ann. Rheum. Dis.* **80**, 413–422 (2021).
32. A. P. Kusumbe, S. K. Ramasamy, R. H. Adams, Coupling of angiogenesis and osteogenesis by a specific vessel subtype in bone. *Nature* **507**, 323–328 (2014).

33. Y. Hu, H. Wu, T. Xu, Y. Wang, H. Qin, Z. Yao, P. Chen, Y. Xie, Z. Ji, K. Yang, Y. Chai, X. Zhang, B. Yu, Z. Cui, Defactinib attenuates osteoarthritis by inhibiting positive feedback loop between H-type vessels and MSCs in subchondral bone. *J. Orthop. Transl.* **24**, 12–22 (2020).
34. H. Kofoed, Hemodynamics and metabolism in arthrosis: Studies in the rabbit knee. *Acta Orthop. Scand.* **57**, 119–122 (1986).
35. H. Kofoed, Synovitis causes hypoxia and acidity in synovial fluid and subchondral bone. *Injury* **17**, 391–394 (1986).
36. J. A. Spencer, F. Ferraro, E. Roussakis, A. Klein, J. Wu, J. M. Runnels, W. Zaher, L. J. Mortensen, C. Alt, R. Turcotte, R. Yusuf, D. Côté, S. A. Vinogradov, D. T. Scadden, C. P. Lin, Direct measurement of local oxygen concentration in the bone marrow of live animals. *Nature* **508**, 269–273 (2014).
37. D. G. G. Ruiz, D. J. E. Garcia, E. Stigen, K. B. Lund, M. Popa, B. Davidson, M. M. Safont, C. B. Rygh, H. Espedal, T. M. Barrett, B. E. Haug, E. McCormack, Repurposing ^{18}F-FMISO as a PET tracer for translational imaging of nitroreductase-based gene directed enzyme prodrug therapy. *Theranostics* **11**, 6044–6057 (2021).
38. W. Yu, F. Qiao, X. Su, D. Zhang, H. Wang, J. Jiang, H. Xu, ^{18}F-HX4/^{18}F-FMISO-based micro PET for imaging of tumor hypoxia and radiotherapy-associated changes in mice. *Biomed. Pharmacother.* **119**, 109454 (2019).
39. S. Hu, C. Zhang, L. Ni, C. Huang, D. Chen, K. Shi, H. Jin, K. Zhang, Y. Li, L. Xie, M. Fang, G. Xiang, X. Wang, J. Xiao, Stabilization of HIF-1α alleviates osteoarthritis via enhancing mitophagy. *Cell Death Dis.* **11**, 481 (2020).
40. W. Bouaziz, J. Sigaux, D. Modrowski, C. Devignes, T. Funck-Brentano, P. Richette, H. Ea, S. Provot, M. Cohen-Solal, E. Haÿ, Interaction of HIF1α and β-catenin inhibits matrix metalloproteinase 13 expression and prevents cartilage damage in mice. *Proc. Natl. Acad. Sci. U.S.A.* **113**, 5453–5458 (2016).
41. F. J. Zhang, W. Luo, G. H. Lei, Role of HIF-1α and HIF-2α in osteoarthritis. *Joint Bone Spine* **82**, 144–147 (2015).
42. M. Li, J. Ning, J. Wang, Q. Yan, K. Zhao, X. Jia, SETD7 regulates chondrocyte differentiation and glycolysis via the Hippo signaling pathway and HIF-1α. *Int. J. Mol. Med.* **48**, 210 (2021).
43. J. Bohensky, I. M. Shapiro, S. Leshinsky, S. P. Terkhorn, C. S. Adams, V. Srinivas, HIF-1 regulation of chondrocyte apoptosis: Induction of the autophagic pathway. *Autophagy* **3**, 207–214 (2007).
44. K. Okada, D. Mori, Y. Makii, H. Nakamoto, Y. Murahashi, F. Yano, S. H. Chang, Y. Taniguchi, H. Kobayashi, H. Semba, N. Takeda, W. Piao, K. Hanaoka, T. Nagano, S. Tanaka, T. Saito, Hypoxia-inducible factor-1 alpha maintains mouse articular cartilage through suppression of NF-κB signaling. *Sci. Rep.* **10**, 5425 (2020).
45. C. Zhang, F. Yang, R. Cornelia, W. Tang, S. Swisher, H. Kim, Hypoxia-inducible factor-1 is a positive regulator of Sox9 activity in femoral head osteonecrosis. *Bone* **48**, 507–513 (2011).
46. R. H. Das, G. J. van Osch, M. Kreukniet, J. Oostra, H. Weinans, H. Jahr, Effects of individual control of pH and hypoxia in chondrocyte culture. *J. Orthop. Res.* **28**, 537–545 (2010).
47. W. Wei, Y. Ma, X. Yao, W. Zhou, X. Wang, C. Li, J. Lin, Q. He, S. Leptihn, H. Ouyang, Advanced hydrogels for the repair of cartilage defects and regeneration. *Bioact Mater* **6**, 998–1011 (2021).
48. Y. Hu, X. Li, Q. Zhang, Z. Gu, Y. Luo, J. Guo, X. Wang, Y. Jing, X. Chen, J. Su, Exosome-guided bone targeted delivery of Antagomir-188 as an anabolic therapy for bone loss. *Bioact Mater* **6**, 2905–2913 (2021).
49. Y. Han, J. Yang, W. Zhao, H. Wang, Y. Sun, Y. Chen, J. Luo, L. Deng, X. Xu, W. Cui, H. Zhang, Biomimetic injectable hydrogel microspheres with enhanced lubrication and controllable drug release for the treatment of osteoarthritis. *Bioact. Mater.* **6**, 3596–3607 (2021).
50. H. Song, X. Li, Z. Zhao, J. Qian, Y. Wang, J. Cui, W. Weng, L. Cao, X. Chen, Y. Hu, J. Su, Reversal of osteoporotic activity by endothelial cell-secreted bone targeting and biocompatible exosomes. *Nano Lett.* **19**, 3040–3048 (2019).
51. M. Barben, D. Ail, F. Storti, K. Klee, C. Schori, M. Samardzija, S. Michalakis, M. Biel, I. Meneau, F. Blaser, D. Barthelmes, C. Grimm, Hif1a inactivation rescues photoreceptor degeneration induced by a chronic hypoxia-like stress. *Cell Death Differ.* **25**, 2071–2085 (2018).
52. S. He, M. Wang, Z. Yang, J. Zhang, Y. Zhang, J. Luo, Y. Zhang, Comparison of 18F-FES, 18F-FDG, and 18F-FMISO PET imaging probes for early prediction and monitoring of response to endocrine therapy in a mouse xenograft model of ER-positive breast cancer. *PLOS ONE* **11**, e159916 (2016).
53. W. Yajun, C. Jin, G. Zhengrong, F. Chao, H. Yan, W. Weizong, L. Xiaoqun, Z. Qirong, C. Huiwen, Z. Hao, G. Jiawei, Z. Xinchen, S. Shihao, W. Sicheng, C. Xiao, S. Jiacan, Betaine attenuates osteoarthritis by inhibiting osteoclastogenesis and angiogenesis in subchondral bone. *Front. Pharmacol.* **12**, e723988 (2021).
54. X. Chen, Z. Zhang, Y. Hu, J. Cui, X. Zhi, X. Li, H. Jiang, Y. Wang, Z. Gu, Z. Qiu, X. Dong, Y. Li, J. Su, Lactulose suppresses osteoclastogenesis and ameliorates estrogen deficiency-induced bone loss in mice. *Aging Dis.* **11**, 629–641 (2020).
55. K. P. H. Pritzker, S. Gay, S. A. Jimenez, K. Ostergaard, J. P. Pelletier, P. A. Revell, D. Salter, W. B. van den Berg, Osteoarthritis cartilage histopathology: Grading and staging. *Osteoarthr. Cartilage* **14**, 13–29 (2006).
56. J. Chen, H. Zhang, X. Wu, F. Wang, Y. Wang, Q. Gao, H. Liu, Y. Hu, J. Su, Y. Jing, PTHG2 reduces bone loss in ovariectomized mice by directing bone marrow mesenchymal stem cell fate. *Stem Cells Int.* **2021**, 8546739 (2021).
57. A. Butler, P. Hoffman, P. Smibert, E. Papalexi, R. Satija, Integrating single-cell transcriptomic data across different conditions, technologies, and species. *Nat. Biotechnol.* **36**, 411–420 (2018).
58. E. Z. Macosko, A. Basu, R. Satija, J. Nemesh, K. Shekhar, M. Goldman, I. Tirosh, A. R. Bialas, N. Kamitaki, E. M. Martersteck, J. J. Trombetta, D. A. Weitz, J. R. Sanes, A. K. Shalek, A. Regev, S. A. McCarroll, Highly parallel genome-wide expression profiling of individual cells using nanoliter droplets. *Cell* **161**, 1202–1214 (2015).
59. W. J. Dixon, Efficient analysis of experimental observations. *Annu. Rev. Pharmacol. Toxicol.* **20**, 441–462 (1980).

Acknowledgments: We thank the Shanghai Model Organisms for constructing *Lcp1* knockout mice. We thank the Department of nuclear medicine of Renji hospital affiliated to Shanghai JiaoTong University School of Medicine for providing ^{18}F-FMISO and PET/CT. We thank OBiO Technology (Shanghai) for constructing *Hif1a* knockdown AAV. We thank OE Biotech Company (Shanghai, China) for the supporting of bioinformatics analysis. **Funding:** This work was supported by the State Key Program of National Natural Science Foundation of China (82230071), the Integrated Project of Major Research Plan of National Natural Science Foundation of China (92249303), the National Key R&D Program of China (2018YFC2001500), the National Natural Science Foundation of China (82172098, 81972254, 81871099, and 81901426), the Shanghai Rising Star Program (21QA1412000), and the Shanghai Baoshan Medical Research Program (21-E-67). **Author contributions:** Conceptualization: H.Z., L.W., J.Cu., J.Ch., and X.C. Methodology: H.Z., H.S., C.W., J.Ch., and J.Cu. Investigation: H.Z., S.W., Y.H., X.L., Q.Z., J.G., X.Z., S.S., J.Ch., and T.Z. Visualization: H.Z., S.W., X.L., D.Z., Y.F.H., J.Cu., F.W., and Q.G. Funding acquisition: Y.J., X.C., and J.S. Project administration: Y.J. and X.C. Supervision: Y.J., X.C., and J.S. Writing (original draft): H.Z. and L.W. Writing (review and editing): Y.J., X.C., J.Ch., and J.S. **Competing interests:** J.S., X.C., and H.Z. are inventors on four patent applications related to this work filed by Shanghai Hemai Medical Technology Co. LTD (no. 202210262783.5, filed 17 March 2022; no. 202210262989.8, filed 17 March 2022; no. 202210263025.5, filed 17 March 2022; and no. 202210277280.5, filed 17 March 2022). The authors declare that they have no other competing interests. **Data and materials availability:** All data needed to evaluate the conclusions in the paper are present in the paper and/or the Supplementary Materials. The data for this study have also been deposited in the database Dyrad (URL: https://datadryad.org/stash/share/-2b8LIXWnPtSBgIcN_e0Hn7qNFwQqDYMETYGgQy4J_M).

Submitted 28 February 2022
Accepted 8 March 2023
Published 5 April 2023
10.1126/sciadv.abo7868